Full band all-sky search for periodic gravitational waves in the O1 LIGO data

Citation: Abbott, B. P., et al. "Full Band All-Sky Search for Periodic Gravitational Waves in the O1 LIGO Data." Physical Review D, vol. 97, no. 10, May 2018. © 2018 American Physical Society

As Published: http://dx.doi.org/10.1103/PhysRevD.97.102003

Publisher: American Physical Society

Persistent URL: http://hdl.handle.net/1721.1/116312

Version: Final published version: final published article, as it appeared in a journal, conference proceedings, or other formally published context

Full band all-sky search for periodic gravitational waves in the O1 LIGO data

B. P. Abbott *et al.*[*]
(LIGO Scientific Collaboration and Virgo Collaboration)

(Received 15 February 2018; published 11 May 2018)

We report on a new all-sky search for periodic gravitational waves in the frequency band 475–2000 Hz and with a frequency time derivative in the range of $[-1.0, +0.1] \times 10^{-8}$ Hz/s. Potential signals could be produced by a nearby spinning and slightly nonaxisymmetric isolated neutron star in our Galaxy. This search uses the data from Advanced LIGO's first observational run O1. No gravitational-wave signals were observed, and upper limits were placed on their strengths. For completeness, results from the separately published low-frequency search 20–475 Hz are included as well. Our lowest upper limit on worst-case (linearly polarized) strain amplitude h_0 is $\sim 4 \times 10^{-25}$ near 170 Hz, while at the high end of our frequency range, we achieve a worst-case upper limit of 1.3×10^{-24}. For a circularly polarized source (most favorable orientation), the smallest upper limit obtained is $\sim 1.5 \times 10^{-25}$.

DOI: 10.1103/PhysRevD.97.102003

I. INTRODUCTION

In this paper, we report the results of an all-sky, multi-pipeline search for continuous, nearly monochromatic gravitational waves in data from Advanced LIGO's first observational run (O1) [1]. The search covered signal frequencies from 475 through 2000 Hz and frequency derivatives over the range $[-1.0, +0.1] \times 10^{-8}$ Hz/s.

Rapidly rotating neutron stars in our Galaxy could generate detectable continuous gravitational waves via various processes. For example, crustal deformation from cooling accompanied by cracking or magnetic field energy buried below the crust could lead to the nonaxisymmetry necessary for emission. See Refs. [2,3] for recent, comprehensive reviews of continuous gravitational-wave emission mechanisms from neutron stars. Detection of such radiation, combined with a campaign of electromagnetic observations of the same source, could yield valuable insight into the structure of neutron stars and into the equation of state of matter under extreme conditions.

A number of searches for periodic gravitational waves from isolated neutron stars have been carried out previously in LIGO and Virgo data [4–32]. These searches have included coherent searches for continuous wave (CW) gravitational radiation from known radio and x-ray pulsars, directed searches for known stars or locations having unknown signal frequencies, and spotlight or all-sky searches for signals from unknown sources. None of those searches has found any signals, establishing limits on strength of any putative signals. No previous search for continuous waves covered the band 1750–2000 Hz.

[*]Full author list given at the end of the article.

Three search methods were employed to analyze O1 data:

(i) The *PowerFlux* pipeline has been used in previous searches of LIGO's S4, S5, and S6 and O1 runs [15,17,19,22,31] and uses a *loosely coherent* method for following up outliers [33]. A new *universal* statistic [34] provides correct upper limits regardless of the noise distribution of the underlying data, while still showing close to optimal performance for Gaussian data.

The follow-up of outliers uses a newly implemented dynamic programming algorithm similar to the Viterbi method [35] implemented in another recent CW search of Scorpius X-1 [36].

(ii) The *SkyHough* pipeline has been used in previous all-sky searches of the initial LIGO S2, S4 and S5 and Advanced LIGO O1 data [14,15,26,31]. The use of the Hough algorithm makes it more robust than other methods with respect to noise spectral disturbances and phase modeling of the signal [15,37]. Population-based frequentist upper limits are derived from the estimated average sensitivity depth obtained by adding simulated signals into the data.

(iii) The Time-Domain $\mathcal{F}$-statistic pipeline has been used in the all-sky searches of the Virgo VSR1 data [27] and of the low-frequency part of the LIGO O1 data [31]. The core of the pipeline is a coherent analysis of narrow band time-domain sequences with the $\mathcal{F}$-statistic method [38]. Because of heavy computing requirements of the coherent search, the data are divided into time segments of a few days long, which are separately coherently analyzed with the $\mathcal{F}$-statistic. This is followed by a search for coincidences among candidates found in different short time segments

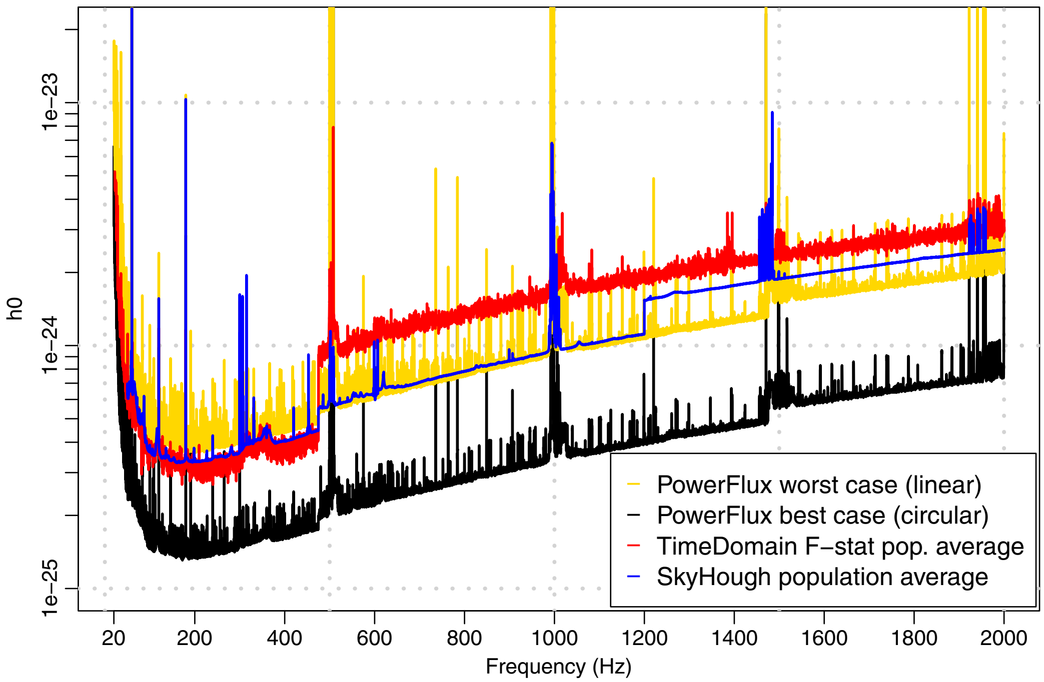

FIG. 1. O1 upper limits. The dimensionless strain (vertical axis) is plotted against signal frequency. Looking at the right side of the plot, the upper (red) curve shows Time Domain F-statistic 95% C.L. population averaged upper limits, the next lower curve (blue) shows maximum population average upper limits from SkyHough, followed by yellow curve showing PowerFlux worst-case (linearly polarized) 95% C.L. upper limits in analyzed bands. PowerFlux upper limits are maximized over sky and all intrinsic signal parameters for each frequency band displayed. The lower (black) curve shows upper limits assuming a circularly polarized source. We include the data from the low-frequency paper [31] to present the entire range 20–2000 Hz. As the computational demands grow with frequencies, each pipeline tunes parameters to reduce computation load. This accounts for jumps in curves at 475, 1200, and 1475 Hz. The SkyHough upper limit curve shows the maximum of the range of different upper limits shown in Fig. 7 with different upper limit values corresponding to different search depths. Because of highly non-Gaussian data, the SkyHough search depths are not expected to be well estimated for each individual search band but are representative of the noise behavior in the entire frequency range. The data for this plot can be found in Ref. [39].

(Ref. [27], Sec. VIII), for a given band. In order to estimate the sensitivity, frequentist upper limits are obtained by injecting simulated signals into the data.

The pipelines present diverse approaches to data analysis, with coherence lengths from 1800 s to a few days, and different responses to line artifacts present in the data.

After following up numerous early stage outliers, no evidence was found for continuous gravitational waves in the O1 data over the band and range of frequency derivatives searched. We therefore present bounds on detectable gravitational radiation in the form of 95% confidence level upper limits (Fig. 1) for worst-case (linear) polarization. The worst-case upper limits apply to any combination of parameters covered by the search. Best-case (circular) upper limits are presented as well, allowing one to compute the maximum distance to detected objects, under certain assumptions. Population average upper limits are produced by SkyHough and Time-Domain $\mathcal{F}$-statistic pipelines.

II. LIGO INTERFEROMETERS AND O1 OBSERVING RUN

The LIGO gravitational-wave network consists of two observatories, one in Hanford, Washington, and the other in Livingston, Louisiana, separated by a 3000 km baseline. During the O1 run, each site housed one suspended interferometer with 4-km-long arms. The interferometer mirrors act as test masses, and the passage of a gravitational wave induces a differential arm length change that is proportional to the gravitational-wave strain amplitude. The Advanced LIGO [40] detectors came online in September 2015 after a major upgrade. While not yet operating at design sensitivity, both detectors reached an instrument noise three to four times lower than ever measured before in their most sensitive frequency band between 100 and 300 Hz [41].

The suspension systems of the optical elements were greatly improved, extending the usable frequency range down to 20 Hz. The use of monolithic suspensions provided for sharper resonances of so-called violin modes, resulting in narrower (in frequency) detector artifacts. An increase in mirror mass has shifted the resonances to the vicinity of 500 Hz, opening up previously contaminated frequency bands.

With these positive effects came some new difficulties: the increase in the number of optical elements resulted in more violin modes as well as new less-well-understood resonances [31].

Advanced LIGO's first observing run occurred between September 12, 2015, and January 19, 2016, from which approximately 77 and 66 days of analyzable data were produced by the Hanford (H1) and Livingston (L1) interferometers, respectively. Notable instrumental contaminants affecting the searches described here included spectral combs of narrow lines in both interferometers, many of which were identified after the run ended and mitigated for future runs. These artifacts included an 8 Hz comb in H1 with the even harmonics (16 Hz comb) being especially strong. This comb was later tracked down to digitization roundoff error in a high-frequency excitation applied to servocontrol the cavity length of the output mode cleaner (OMC). Similarly, a set of lines found to be linear combinations of 22.7 and 25.6 Hz in the L1 data was tracked down to OMC excitation at a still higher frequency, for which digitization error occurred.

A subset of these lines with common origins at the two observatories contaminated the O1 search for a stochastic background of gravitational waves, which relies upon cross-correlation of H1 and L1 data, requiring excision of affected bands [29,42,43].

Although most of these strong and narrow lines are stationary in frequency and hence do not exhibit the Doppler modulations due to the Earth's motion expected for a CW signal from most sky locations, the lines pollute the spectrum for such sources. In sky locations near the ecliptic poles, where a putative CW signal would have little Doppler modulation, the lines contribute extreme contamination for certain signal frequencies. This effect was particularly severe for the low-frequency results in the 20–475 Hz range [31].

III. SIGNAL WAVEFORM

In this paper, we assume a standard model of a spinning nonaxisymmetric neutron star. Such a neutron star radiates circularly polarized gravitational radiation along the rotation axis and linearly polarized radiation in the directions perpendicular to the rotation axis. For the purposes of detection and establishing upper limits, the linear polarization is the worst case, as such signals contribute the smallest amount of power to the detector.

The strain signal template measured by a detector is assumed to be

$$h(t) = h_0\left(F_+(t,\alpha_0,\delta_0,\psi)\frac{1+\cos^2(\iota)}{2}\cos(\Phi(t)) + F_\times(t,\alpha_0,\delta_0,\psi)\cos(\iota)\sin(\Phi(t))\right), \quad (1)$$

where F_+ and $F_\times$ characterize the detector responses to signals with $+$ and $\times$ quadrupolar polarizations [15,17,19], the sky location is described by right ascension α_0 and declination δ_0, the inclination of the source rotation axis to the line of sight is denoted ι, and we use ψ to denote the polarization angle (i.e. the projected source rotation axis in the sky plane).

The phase evolution of the signal is given by

$$\Phi(t) = 2\pi(f_{\mathrm{source}}\cdot(t-t_0) + f^{(1)}\cdot(t-t_0)^2/2) + \phi, \quad (2)$$

with f_{source} being the source frequency and $f^{(1)}$ denoting the first frequency derivative (which, when negative, is termed the "spin-down"). We use t to denote the time in the Solar System barycenter frame. The initial phase ϕ is computed relative to reference time t_0. When expressed as a function of local time of ground-based detectors, Eq. (2) acquires sky-position-dependent Doppler shift terms.

Most natural "isolated" sources are expected to have a negative first frequency derivative, as the energy lost in gravitational or electromagnetic waves would make the source spin more slowly. The frequency derivative can be positive when the source is affected by a strong slowly variable Doppler shift, such as due to a long-period orbit.

IV. POWERFLUX SEARCH FOR CONTINUOUS GRAVITATIONAL RADIATION

A. Overview

This search has two main components. First, the main PowerFlux algorithm [15,17,19,44–46] is run to establish upper limits and produce lists of outliers with signal-to-noise ratio (SNR) greater than 5. Next, the Loosely Coherent detection pipeline [19,33,47] is used to reject or confirm collected outliers.

Both algorithms calculate power for a bank of signal model templates and compute upper limits and signal-to-noise ratios for each template based on comparison to templates with nearby frequencies and the same sky location and spin-down. The input time series is broken into 50%-overlapping long segments with durations shown in Table I, which are then Hann windowed and Fourier transformed. The resulting *short Fourier transforms* (SFTs) are arranged into an input matrix with time and frequency dimensions. The power calculation can be expressed as a bilinear form of the input matrix $\{a_{t,f}\}$:

$$P[f] = \sum_{t_1,t_2} a_{t_1,f+\delta f(t_1)} a^*_{t_2,f+\delta f(t_2)} K_{t_1,t_2,f}. \quad (3)$$

Here, $\delta f(t)$ denotes the detector frame frequency drift due to the effects from both Doppler shifts and the first frequency derivative. The sum is taken over all times t corresponding to the midpoint of the short Fourier transform time interval. The kernel $K_{t_1,t_2,f}$ includes the contribution of time-dependent SFT weights, antenna response, signal polarization parameters, and relative phase terms [33,47].

TABLE I. PowerFlux analysis pipeline parameters. Starting with stage 1, all stages used the Loosely Coherent algorithm for demodulation. The sky and frequency refinement parameters are relative to values used in the semicoherent PowerFlux search. The 7200 s SFTs used for analysis of 20–475 Hz range were too computationally expensive for higher frequencies, and smaller 3600 and 1800 s SFTs were used instead. The breakpoints 475 Hz and 1475 Hz break points were chosen so that the more computationally expensive range ends just before heavy instrumental artifacts due to violin modes of mirrors and the beam splitter.

Stage	Instrument sum	Phase coherence (rad)	Spindown step (Hz/s)	Sky refinement	Frequency refinement	SNR increase (%)
	20–475 Hz frequency range, 7200 s SFTs, 0.0625 Hz frequency bands					
0	Initial/upper limit semicoherent		1×10^{-10}	1	1/2	
1	Incoherent	$\pi/2$	1.0×10^{-10}	1/4	1/8	20
2	Coherent	$\pi/2$	5.0×10^{-11}	1/4	1/8	10
3	Coherent	$\pi/4$	2.5×10^{-11}	1/8	1/16	10
4	Coherent	$\pi/8$	5.0×10^{-12}	1/16	1/32	7
	475–1475 Hz frequency range, 3600 s SFTs, 0.125 Hz frequency bands					
0	Initial/upper limit semicoherent		1×10^{-10}	1	1/2	
1	Coherent	$\pi/2$	3.0×10^{-10}	1/4	1/8	40
2	Coherent	$\pi/4$	1.5×10^{-10}	1/8	1/8	12
3	Coherent	$\pi/8$	7.5×10^{-11}	1/8	1/16	0
	1475–2000 Hz frequency range, 1800 s SFTs, 0.25 Hz frequency bands					
0	Initial/upper limit semicoherent		1×10^{-10}	1	1/2	
1	Coherent	$\pi/2$	3.0×10^{-10}	1/4	1/8	40
2	Coherent	$\pi/4$	1.5×10^{-10}	1/8	1/8	12
3	Coherent	$\pi/8$	7.5×10^{-11}	1/8	1/16	8

The main semicoherent PowerFlux algorithm uses a kernel with main diagonal terms only that is easy to make computationally efficient. The Loosely Coherent algorithms increase coherence time while still allowing for controlled deviation in phase [33]. This is done using more complicated kernels that increase the effective coherence length.

The effective coherence length is captured in a parameter δ, which describes the amount of phase drift that the kernel allows between SFTs, with $\delta = 0$ corresponding to a fully coherent case and $\delta = 2\pi$ corresponding to incoherent power sums.

Depending on the terms used, the data from different interferometers can be combined incoherently (such as in stage 0; see Table I) or coherently (as used in stage 2 or 3). The coherent combination is more computationally expensive but provides much better parameter estimation.

The upper limits (Fig. 1) are reported in terms of the worst-case value of h_0 (which applies to linear polarizations with $\iota = \pi/2$) and for the most sensitive circular polarization ($\iota = 0$ or π). As described in the previous paper [19], the pipeline does retain some sensitivity, however, to non-general-relativity GW polarization models, including a longitudinal component, and to slow amplitude evolution. A search for non-general-relativity GW signals from known pulsars is described in Ref. [48].

The 95% C.L. upper limits (see Fig. 1) produced in the first stage are based on the overall noise level and largest outlier in strain found for every combination of sky position, spin-down, and polarization in each frequency band in the first stage of the pipeline. These bands are analyzed by separate instances of PowerFlux [19], and their widths vary depending on the frequency range (see Table I). A follow-up search for detection is carried out for high-SNR outliers found in the first stage.

B. Universal statistics

The improvements in detector noise for Advanced LIGO included extension of the usable band down to ∼20 Hz, allowing searches for lower-frequency sources than previously possible with LIGO data. As discussed above, however, a multitude of spectral combs contaminated the data, and in contrast to the 23 month S5 Science Run and 15 month S6 Science Runs of initial LIGO, the 4 month O1 run did not span the Earth's full orbit, which means the Doppler shift magnitudes from the Earth's motion are reduced, on the whole, compared to those of the earlier runs. In particular, for certain combinations of sky location, frequency, and spin-down, a signal can appear relatively stationary in frequency in the detector frame of reference, with the effect being most pronounced for low signal frequencies as noted in Ref. [31].

To allow robust analysis of the entire spectrum, we use in this analysis the Universal statistic algorithm [34] for establishing upper limits. The algorithm is derived from the Markov inequality and shares its independence from the underlying noise distribution. It produces upper limits less than 5% above optimal in the case of Gaussian noise. In non-Gaussian bands, it can report values larger than what

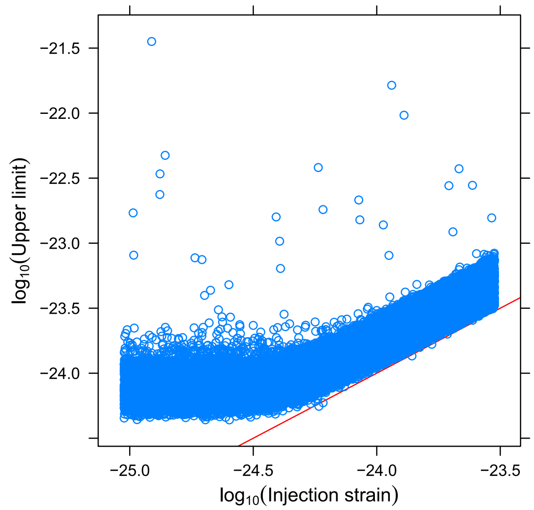

FIG. 2. PowerFlux upper limit validation. Each point represents a separate injection in the 475–1475 Hz frequency range. Each established upper limit (vertical axis) is compared against the injected strain value (horizontal axis, red line). The plot for the high-frequency range 1475–2000 Hz is very similar and not included in this paper.

would be obtained if the distribution were known, but the upper limits are always at least 95% valid. Figure 2 shows results of an injection run performed as described in Ref. [19]. Correctly established upper limits lie above the red line.

C. Detection pipeline

The outlier follow-up used in Refs. [19,22] has been extended with additional stages (see Table I) to winnow the larger number of initial outliers, expected because of non-Gaussian artifacts and the larger initial search space. This paper uses fewer stages than Ref. [31] because of the use of a dynamic programming algorithm which allowed proceeding straight to coherent combinations of interferometer data.

The initial stage (marked 0) scans the entire sky with a semicoherent algorithm that computes weighted sums of powers of Hann-windowed SFTs. These power sums are then analyzed to identify high-SNR outliers. A separate algorithm uses Universal statistics [34] to establish upper limits. The entire data set is partitioned into three stretches of approximately equal length, and power sums are produced independently for any contiguous combinations of these stretches. As in Refs. [22,25], the outlier identification is performed independently in each contiguous combination.

High-SNR outliers are subject to a coincidence test. For each outlier with SNR > 7 in the combined H1 and L1 data, we require there to be outliers in the individual detector data of the same sky area that had SNR > 5, matching the parameters of the combined-detector outlier within 167 μHz in frequency (333 μHz for the 1475–2000 Hz band) and 6×10^{-10} Hz/s in spin-down. The combined-detector SNR is required to be above both single-detector SNRs. The identified outliers using combined data are then passed to a follow-up stage using the Loosely Coherent algorithm [33] with progressively tighter phase coherence parameters δ and improved determination of frequency, spin-down, and sky location.

A new feature of this analysis is the use of a dynamic programming algorithm similar to the Viterbi method [35,36] in follow-up stages. The three stretches are each partitioned into four parts (forming 12 parts total). Given a sequence of parts, the weighted sum is computed by combining precomputed sums for each part, but the frequency is allowed to jump by at most one subfrequency bin. To save space, the weighted sums are maximized among all sequence combinations that have the same ending frequency bin. The use of dynamic programming made the computation efficient. Because the resulting power sum is a maximum of many power sums, the statistics are slightly altered and are not expected to be Gaussian. They are sufficiently close to Gaussian, however, and the Universal statistic algorithm works well with these data, even though it was optimized for a Gaussian case. The follow-up stages use the SNR produced by the same algorithm.

Allowing variation between the stretches widens the range of acceptable signals, making the search more robust. The greatest gains from this improvement, though, are in computational speed, as we can use coarser spin-down steps and other parameters with only a small loss in sensitivity. This was critical for completing the Monte Carlo simulations that verify effectiveness of the pipeline (Fig. 3).

As the initial stage 0 sums only powers, it does not use the relative phase between interferometers, which results in some degeneracy between sky position, frequency, and spin-down. The first Loosely Coherent follow-up stage combines interferometer powers coherently and demands greater temporal coherence (smaller δ), which should boost the SNR of viable outliers by at least 40%. Subsequent stages provide tighter bounds on the outlier location. Surviving outliers are passed to the Einstein@Home pipeline [30,32].

The testing of the pipeline was performed by comprehensive simulations in each frequency range. Injection recovery efficiencies from simulations covering the 475–1475 Hz range are shown in Fig. 3. The simulations for higher frequencies 1475–2000 Hz produced a very similar plot, which is not shown here. We want to highlight that simulations included highly contaminated regions such as violin modes and demonstrate the algorithm's robustness to extreme data.

In order to maintain low false dismissal rates, the follow-up pipeline used wide tolerances in associating outliers

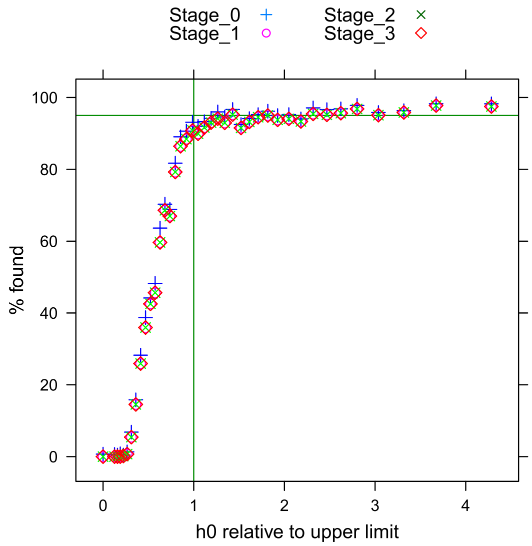

FIG. 3. PowerFlux injection recovery. The injections were performed in the 475–1475 Hz band. The injected strain divided by the upper limit in this band computed without injection is shown on the horizontal axis. The percentage of surviving injections is shown on the vertical axis, with a horizontal line drawn at the 95% level. Stage 0 is the output of the coincidence test after the initial semicoherent search. The plot for high-frequency range 1475–2000 Hz is very similar and not included here.

between stages. For example, when transitioning from the semicoherent stage 0 to the Loosely Coherent stage 1, the effective coherence length increases by a factor of 4. The average true signal SNR should then increase by more than 40%. An additional 40% is expected from the coherent combination of data between interferometers. But the threshold used in follow-up is only 40%, which accommodates unfavorable noise conditions, template mismatch, detector artifacts, and differences in the detector duty cycle.

Our recovery criteria demand that an outlier close to the true injection location (within 3 mHz in frequency f, 7×10^{-11} Hz/s in spin-down, and [6 rad Hz/f, 12 rad Hz/f] for [475 – 1475 Hz, 1475 – 2000 Hz] in sky location) be found and successfully pass through all stages of the detection pipeline. As each stage of the pipeline passes only outliers with an increase in the SNR, signal injections result in outliers that strongly stand out above the background.

The follow-up code was verified to recover 90% of injections at or above the upper limit level for a uniform distribution of injection frequencies (Fig. 3). This fraction rises with injection strength. Compared with similar PowerFlux plots in earlier papers, we do not reach 95% injection recovery right away. This is due to uneven sensitivity between interferometers (our coincidence test demands an outlier be marginally seen in individual interferometers), as well as heavily contaminated data. We note that this is still a 95% upper limit: if a louder signal had actually been present, we would have set a higher upper limit 95% of the time, even if we could only *detect* the signal 90% of the time.

V. SKYHOUGH SEARCH FOR CONTINUOUS GRAVITATIONAL RADIATION

A. Overview

The SkyHough search method is described in detail in Refs. [26,49–51] and was also used in the previous low-frequency O1 search [31]. The search consists primarily of two main steps. First, the data from the two LIGO interferometers are analyzed in separate all-sky searches for continuous gravitational-wave signals, using a Hough transform algorithm that produces sets of top lists of the most significant events. In the second step, coincidence requirements on candidates are imposed.

In the first step, an implementation of the weighted Hough transform, SkyHough [26,50], is used to map points from the digitized time-frequency plane of the data, called the "peak gram," into the space of the source parameters. The algorithm searches for signals of which the frequency evolution fits the pattern produced by the Doppler shift and spin down in the time-frequency plane of the data. In this case, the Hough number count, n, is the sum of the ones and zeroes of the peak gram weighted using the detector antenna pattern and the noise level. A useful detection statistic is the *significance* (or critical ratio) and is given by

$$s = \frac{n - \langle n \rangle}{\sigma}, \tag{4}$$

where $\langle n \rangle$ and σ are the expected mean and standard deviation of the Hough number count for pure noise.

The analysis of the SkyHough search presented here has not identified any convincing continuous gravitational-wave signal. Hence, we proceed to set upper limits on the maximum intrinsic wave strain h_0 that is consistent with our observations for a population of signals described by an isolated triaxial rotating neutron star. As in previous searches, we set all-sky population-based frequentist upper limits, that are given in different frequency sub-bands.

B. Detection pipeline

As was done in the previous low-frequency Advanced-LIGO O1 search [31], covering frequencies up to 475 Hz, this search method uses calibrated detector $h(t)$ data to create 1800 s Tukey-windowed SFTs, where each SFT is created from a segment of detector data that is at least 1800 s long. From this step, 3684 and 3007 SFTs are created for H1 and L1, respectively. SFT data from a single interferometer are analyzed by setting a threshold of 1.6 on the normalized power and then creating a peak gram (a collection of 0s and 1s). The averaged spectrum is determined via a running-median estimation [15] which uses 50 frequency bins to each side of the current bin.

The SkyHough search analyzes 0.1 Hz bands over the frequency interval 475–2000 Hz and frequency time derivatives in the range $[-1.0, +0.1] \times 10^{-8}$ Hz/s and covers the entire sky. A uniform grid spacing, equal to the size of a SFT frequency bin, $\delta f = 1/T_{\rm coh} = 5.556 \times 10^{-4}$ Hz, is chosen, where $T_{\rm coh}$ is the duration of a SFT. The resolution in the first frequency derivative, $\delta \dot{f}$, is given by the smallest value of $\dot{f}$ for which the intrinsic signal frequency does not drift by more than one frequency bin during the total observation time $T_{\rm obs}$: $\delta \dot{f} = \delta f / T_{\rm obs} \sim 4.95 \times 10^{-11}$ Hzs^{-1}. This yields 203 spin-down values and 21 spin-up values for each frequency. The angular spacing of the sky grid points, $\delta\theta$ (in radians), is frequency dependent, with the number of templates increasing with frequency, as given by Eq. (4.14) of Ref. [49],

$$\delta\theta = \frac{10^4 \delta f}{f N_p}, \tag{5}$$

where the pixel factor N_p is a variable that can be manually changed to accommodate the desired sky resolution and consequently the computational cost of the search. The scaling factor of 10^4 accounts for the maximum sky-position-dependent frequency modulation $v/c \sim 10^{-4}$ due to Earth's orbit. For the Initial-LIGO S5 search, N_p was set to 0.5 [26], while in the previous low-frequency Advanced-LIGO O1 search [31], N_p was set to 2, thus increasing the sky resolution by a factor of 16.

For each 0.1 Hz frequency band, the parameter space is split further into 209 subregions of the sky. For every sky region and frequency band, the analysis program compiles a list of the 1000 most significant candidates (those with the highest critical ratio values). A final list of the 1000 most significant candidates for each 0.1 Hz frequency band is constructed, with no more than 300 candidates from a single sky region. This procedure reduces the influence of instrumental spectral disturbances that affect specific sky regions.

As the number of sky positions in an all-sky search increases with the square of the frequency, the computational cost becomes larger for the highest frequencies. In order to perform this SkyHough all-sky search within the allocated computational budget, the search presented here is split in two different bands: from 475 to 1200 Hz and from 1200 to 2000 Hz. The pixel factor N_p is set equal to 2 for the 475–1200 Hz band and equal to 0.5 for 1200–2000 Hz, thus performing a lower sky grid resolution search at higher frequencies. Of course, these parameter choices, the duration of the SFTs, sky resolution, and the size of the top list per frequency band have implications on the final sensitivity of the search itself compared to what could have been achieved. Around 1200 Hz, we estimate that the sensitivity would have been 20% better if the pixel factor N_p had remained 2, as can be inferred from Fig. 7.

C. Postprocessing stage

The postprocessing of the top lists for each 0.1 Hz band consists of the following steps:

(i) Search for coincident candidates among the H1 and L1 data sets, using a coincidence window of $d_{\rm SH} < \sqrt{14}$. This dimensionless quantity is defined as

$$d_{\rm SH} = \sqrt{(\Delta f/\delta f)^2 + (\Delta \dot{f}/\delta \dot{f})^2 + (\Delta\theta/\delta\theta)^2} \tag{6}$$

to take into account the distances in frequency, spin down, and sky location with respect to the grid resolution in parameter space. Here, $\Delta\theta$ is the sky angle separation. Each coincidence pair is then characterized by its harmonic mean significance value and a center in parameter space: the mean weighted value of frequency, spin down, and sky location obtained by using their corresponding individual significance values.

(ii) The surviving coincidence pairs are clustered, using the same coincidence window of $d_{\rm SH} < \sqrt{14}$ applied to the coincidence centers. Each coincident candidate can belong to only a single cluster, and an element belongs to a cluster if there exists at least another element within that distance. Only the highest ranked cluster, if any, will be selected for each 0.1 Hz band. Clusters are ranked based on their mean significance value, but where all clusters overlapping with a known instrumental line are ranked below any cluster with no overlap. A cluster is always selected for each of the 0.1 Hz bands that had coincidence candidates. In most cases, the cluster with the largest mean significance value coincides also with the one containing the highest individual value.

Clusters were marked if they overlapped with a list of known instrumental lines. To perform this veto, we consider the frequency interval derived from frequency evolution given by the f and $\dot{f}$ values of the center of the cluster together with its maximum Doppler shift and check if the resulting frequency interval overlaps with the frequency of a known line.

These steps (i)–(ii) take into account the possibility of coincidences and formation of clusters across boundaries of consecutive 0.1 Hz frequency bands.

(iii) Based on previous studies [37], we require that interesting clusters must have a minimum population of 2; otherwise, they are discarded. This is similar to the "occupancy veto" described in Ref. [52].

The remaining candidates are manually examined. In particular, outliers are also discarded if the frequency span of the cluster coincides with the list of instrumental lines described in Sec. II or if there are obvious spectral disturbances associated with one of the detectors. Multidetector searches, as those described in Ref. [31], are also performed to verify the consistency of a possible signal, and surviving outliers are passed to the Einstein@Home pipeline [30,32].

D. Upper limit computation

As in previous searches [26,31], we set a population-based frequentist upper limit at the 95% C.L. Upper limits are derived for each 0.1 Hz band from the estimated average sensitivity depth, in a way similar to the procedure used in the Einstein@Home searches [23,30].

For a given signal strength h_0, the sensitivity depth is defined as

$$\mathcal{D} \coloneqq \frac{\sqrt{S_h}}{h_0} [1/\sqrt{\mathrm{Hz}}]. \tag{7}$$

Here, S_n is the maximum over both detectors of the power spectral density of the data, at the frequency of the signal. S_n is estimated as the power-2 mean value, $(\sum_{i=1}^{N} (S_k^{(i)})^{-2}/N)^{-2}$, across the different noise levels $S_k^{(i)}$ of the different N SFTs.

Two different values of average depth are obtained for the 475–1200 and 1200–2000 Hz frequency bands, respectively, consistent with the change in the sky grid resolution during the search. The depth values corresponding to the averaged all-sky 95% confidence detection efficiency are obtained by means of simulated periodic gravitational-wave signals added into the SFT data of both detectors H1 and L1 in a limited number of frequency bands. In those bands, the detection efficiency, i.e., the fraction of signals that are considered detected, is computed as a function of signal strength h_0 expressed by the sensitivity depth.

For the 475–1200 Hz lower-frequency band, 18 different 0.1 Hz bands were selected with the following starting frequencies: [532.4, 559.0, 580.2, 646.4, 658.5, 678.0, 740.9, 802.4, 810.2, 865.3, 872.1, 935.7, 972.3, 976.3, 1076.3, 1081.0, 1123.4, 1186.0] Hz. These bands were chosen to be free of known spectral disturbances in both detectors, with no coincidence candidates among the H1 and L1 data sets, and scattered over the whole frequency band. In all these selected bands, we generated nine sets of 400 signals each, with fixed sensitivity depth in each set and random parameters $(f, \alpha, \delta, \dot{f}, \varphi_0, \psi, \cos\iota)$. Each signal was added into the data of both detectors, and an analysis was done using the SkyHough search pipeline over a frequency band of 0.1 Hz and the full spin-down range, but covering only one sky patch. For this sky patch, a list of 300 loudest candidates was produced. Then, we imposed a threshold on significance, based on the minimum significance found in the all-sky search in the corresponding 0.1 Hz band before any injections. The postprocessing was then done using the same parameters used in the search, including the population veto. A signal was considered detected if the center of the selected cluster, if any, lay within a distance $d_{\mathrm{SH}} < 13$ from the real injected value. This window was chosen based on previous studies [37] and prevented miscounts due to noise fluctuations or artifacts.

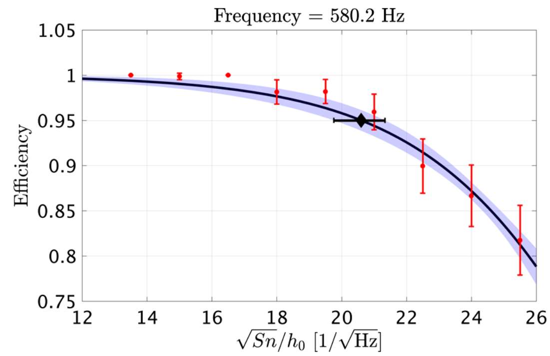

FIG. 4. Detection efficiency as a function of depth obtained for the 0.1 Hz frequency band starting at 580.2 Hz. Each red dot corresponds to a set of 400 signal injections, and error bars on the data points represent the $2\sigma_E$ standard binomial error. The (black) solid line corresponds to the fitted sigmoid curve, and the (blue) shaded envelope corresponds to the $2\sigma_F$ calculated according to Eq. (10). The diamond shows the depth value corresponding to the 95% detection efficiency, $\mathcal{D}^{95\%}$, along with the $2\sigma_F$ uncertainty in black markers.

For the 1200–2000 Hz frequency band, the following 18 different 0.1 Hz bands were selected: [1248.7, 1310.6, 1323.5, 1334.4, 1410.3, 1424.6, 1450.2, 1562.6, 1580.4, 1583.2, 1653.2, 1663.6, 1683.4, 1704.3, 1738.2, 1887.4, 1953.4, 1991.5] Hz. The same procedure described above was applied to these bands.

We collected the results from the two sets of 18 frequency bands, and for each frequency, the detection

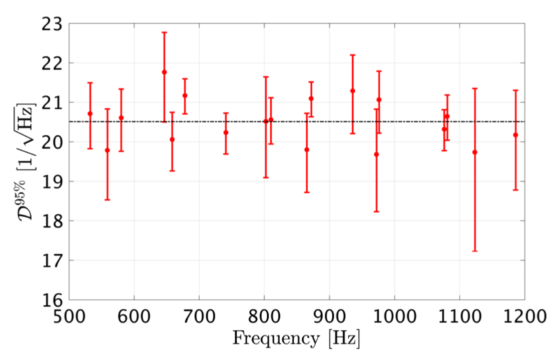

FIG. 5. Depth values corresponding to the 95% detection efficiency, $\mathcal{D}^{95\%}$, obtained for 18 0.1 Hz frequency bands between 475 and 1200 Hz, along with their corresponding $2\sigma_F$ uncertainties from the sigmoid fit in red markers. The average of the measured depths at different frequencies is $\langle\mathcal{D}^{95\%}\rangle_{\mathrm{Low}} = 20.5\ \mathrm{Hz}^{-1/2}$.

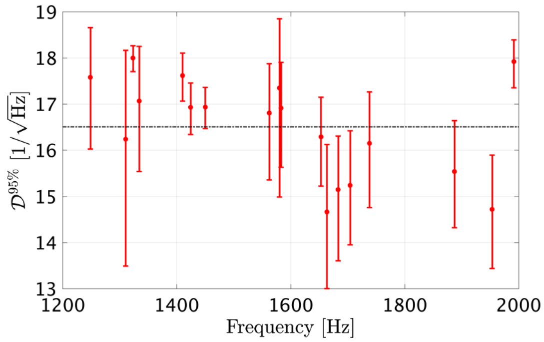

FIG. 6. Depth values corresponding to the 95% detection efficiency, $\mathcal{D}^{95\%}$, obtained for 18 0.1 Hz frequency bands between 1200 and 2000 Hz, along with their corresponding $2\sigma_F$ uncertainties in red markers. The average of the measured depths at different frequencies is $\langle\mathcal{D}^{95\%}\rangle_{\text{High}} = 16.5\ \text{Hz}^{-1/2}$.

efficiency E versus depth $\mathcal{D}$ values was fitted to a sigmoid function of the form

$$E(\mathcal{D}) = 1 - \frac{1}{1 + \exp(b(\mathcal{D} - a))}, \quad (8)$$

using the nonlinear regression algorithm NLINFIT provided by MATLAB. Since the detection rate follows a binomial distribution, each data point was weighted by the standard σ_E error given by

$$\sigma_E = \sqrt{\frac{E(1-E)}{N_I}}, \quad (9)$$

where N_I is the number of injections performed. From the estimated coefficients a and b along with the covariance matrix C, we estimated the σ_F envelope on the fit given by

$$\sigma_F = \pm\sqrt{(\partial_a E)^2 C_{aa} + 2(\partial_a E)(\partial_b E)C_{ab} + (\partial_b E)^2 C_{bb}}, \quad (10)$$

where $\partial_a E$ and $\partial_b E$ indicate partial derivatives with respect to the coefficients a and b of the sigmoid function (8), and derived the corresponding depth at the 95% detection efficiency, $\mathcal{D}^{95\%}$, as illustrated in Fig. 4.

Figures 5 and 6 show the obtained depth values for each frequency corresponding to the 95% efficiency level, $\mathcal{D}^{95\%}$, together with their 2σ uncertainty $\delta\mathcal{D}^{95\%} = 2\sigma_F$.

As a representative of the sensitivity depth of the search, we took the average of the measured depths for each of the two sets of 18 different frequencies. This yielded $\langle\mathcal{D}^{95\%}\rangle_{\text{Low}} = 20.5\ \text{Hz}^{-1/2}$ for the lower 475–1200 Hz band and $\langle\mathcal{D}^{95\%}\rangle_{\text{High}} = 16.5\ \text{Hz}^{-1/2}$ for the higher 1200–2000 Hz band, being the range of variation observed on the measured sensitivity depth of individual frequency bands with respect to the averaged values of 7.4% and 15%, respectively.

The 95% confidence upper limit on h_0 for undisturbed bands can then be derived by simply scaling the power spectral density of the data, $h_0^{95\%} = \sqrt{S_n}/\mathcal{D}^{95\%}$. The computed upper limits are shown in Fig. 7 together with their uncertainty introduced by the estimation procedure. No limits have been placed in 25 0.1 Hz bands in which coincident candidates were detected, as this scaling

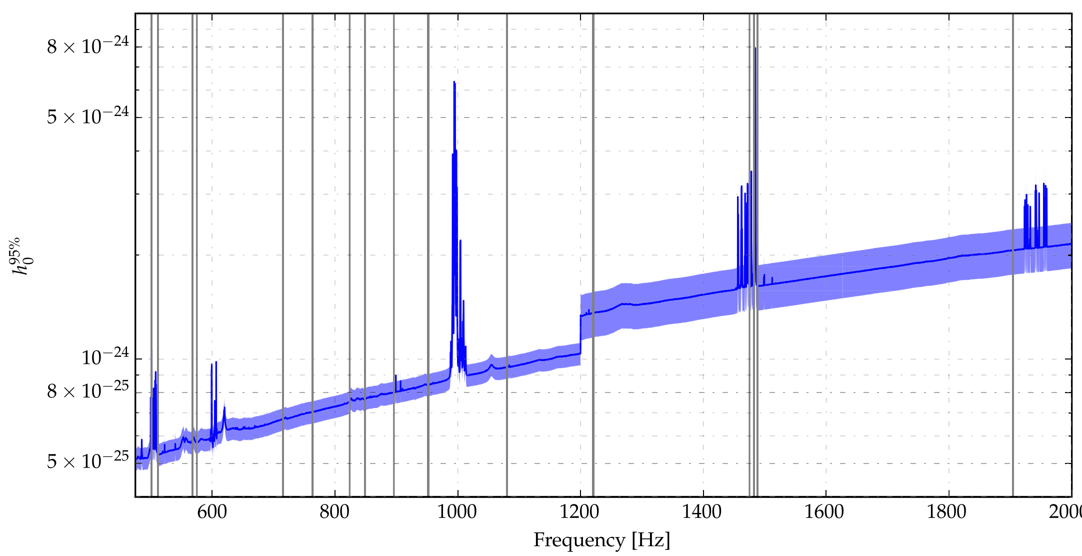

FIG. 7. SkyHough O1 upper limits. The solid (blue) line shows the averaged 95% C.L. upper limits on the gravitational wave amplitude for every analyzed 0.1 Hz band. The vertical (grey) lines indicate 25 0.1 Hz bands in which outliers were found and consequently no upper limits were set. The lighter region around the upper limit represents the 7.4% and 15% uncertainty levels. The jump in sensitivity and uncertainty at 1200 Hz corresponds to the decrease in the sky grid resolution during the search, tuned to reduce the computational load.

procedure can have larger errors in those bands due to the presence of spectral disturbances.

VI. TIME-DOMAIN $\mathcal{F}$-STATISTIC SEARCH FOR CONTINUOUS GRAVITATIONAL RADIATION

The Time-Domain $\mathcal{F}$-statistic search method uses the algorithms described in Refs. [27,38,53,54] and has been applied to an all-sky search of VSR1 data [27] and to the low-frequency part of the LIGO O1 data [31].

The main tool is the $\mathcal{F}$-statistic [38] by which one can search coherently the data over a reduced parameter space consisting of signal frequency, its derivatives, and the sky position of the source. The $\mathcal{F}$-statistic eliminates the need to sample over the four remaining parameters [see Eqs. (1) and (2)]: the amplitude h_0, the inclination angle ι, the polarization angle ψ, and the initial phase ϕ. Once a signal is identified, the estimates of those four parameters are obtained from analytic formulas. However, a coherent search over the whole 120-days-long LIGO O1 data set is computationally prohibitive, and we need to apply a semicoherent method, which consists of dividing the data into shorter time-domain segments. The short time-domain data are analyzed coherently with the $\mathcal{F}$-statistic. Then, the output from the coherent search from time-domain segments is analyzed by a different, computationally manageable method. Moreover, to reduce the computer memory required to do the search, the data are divided into narrow band segments that are analyzed separately. Thus, our search method consists primarily of two parts. The first part is the coherent search of narrow band, time-domain segments. The second part is the search for coincidences among the candidates obtained from the coherent search. The pipeline is described in Sec. IV of Ref. [31] (see also Fig. 13 of Ref. [31] for the flow chart of the pipeline). The same pipeline is used in the high-frequency analysis except that a number of parameters of the search are different. The choice of parameters was motivated by the requirement to make the search computationally manageable.

As in the low-frequency search, the data are divided into overlapping frequency bands of 0.25 Hz. As a result, the band $[475 - 2000]$ Hz has 6300 frequency bands. The time series is divided into segments, called frames, of two sidereal days long each, instead of six sidereal days as in the low-frequency search. For O1 data, which are over 120 days long, we obtain 60 time frames. Each 2 day narrow band segment contains $N = 86164$ data points. The O1 data have a number of nonscience data segments. The values of these bad data are set to zero. For this analysis, we choose only segments that have a fraction of bad data less than $1/3$ in both H1 and L1 data. This requirement results in 20 2-day-long data segments for each band. Consequently, we have 126,000 data segments to analyze. These segments are analyzed coherently using the $\mathcal{F}$-statistic defined by Eq. (9) of Ref. [27]. We set a fixed threshold for the $\mathcal{F}$-statistic of $\mathcal{F}_0 = 16$ (in the low-frequency search, the threshold was set to 14.5) and record the parameters of all threshold crossings, together with the corresponding values of the signal-to-noise ratio ρ,

$$\rho = \sqrt{2(\mathcal{F} - 2)}. \tag{11}$$

Parameters of the threshold crossing constitute a candidate signal.

At this first stage, we also veto candidate signals overlapping with the instrumental lines identified by independent analysis of the detector data.

For the search, we use a four-dimensional grid of templates (parametrized by frequency, spin down, and two more parameters related to the position of the source in the sky) constructed in Sec. 4 of Ref. [54], which belongs to the family S_1 of grids considered in Ref. [54]. The grid's minimal match (MM) is $\mathrm{MM} = 1/2$. It is considerably looser than in the low-frequency search where the parameter MM was chosen to be $\sqrt{3}/2$. The quality of a covering of space by a lattice of identical hyperspheres is expressed by the covering thickness θ, which is defined as the average number of hyperspheres that contain a point in the space. In four dimensions, the optimal lattice covering, i.e. having the minimum, is called $A_4^\star$, and it has the thickness $\theta \cong 1.765529$. The thickness of the new loose grid equals 1.767685, which is only $\sim 0.1\%$ larger than the $A_4^\star$ lattice thickness

In the second stage of the analysis, we search for coincidences among the candidates obtained in the coherent part of the analysis. We use exactly the same coincidence search algorithm as in the analysis of VSR1 data and described in detail in Sec. 8 of Ref. [27]. We search for coincidences in each of the bands analyzed. To estimate the significance of a given coincidence, we use the formula for the false alarm probability derived in the Appendix of Ref. [27]. Sufficiently significant coincidences are called outliers and subjected to further investigation.

The sensitivity of the search is estimated by the same procedure as in the low-frequency search paper (Ref. [31], Sec. IV). The sensitivity is taken to be the amplitude h_0 of the gravitational-wave signal that can be confidently detected. We perform the following Monte Carlo simulations. For a given amplitude h_0, we randomly select the other seven parameters of the signal: ω_0, ω_1, α, δ, ϕ_0, ι, and ψ. We choose frequency and spin-down parameters uniformly over their range and source positions uniformly over the sky. We choose angles ϕ_0 and ψ uniformly over the interval $[0, 2\pi]$ and $\cos\iota$ uniformly over the interval $[-1, 1]$. We add the signal with selected parameters to the O1 data. Then, the data are processed through our pipeline. First, we perform a coherent $\mathcal{F}$-statistic search of each of the data segments where the signal was added. Then, the coincidence analysis of the candidates is performed. The signal is considered to be detected if it is coincident in more than 13 of the 20 time frames analyzed for a given band. We repeat the simulations 100 times. The ratio of numbers of cases in which the signal is detected to the 100 simulations performed for a given h_0 determines the frequentist sensitivity upper limits. We determine the sensitivity of the search in each of the 6300 frequency bands separately. The 95% confidence upper limits for the whole range of frequencies are given in Fig. 9; they follow very well the noise curves of the O1 data that were analyzed. The sensitivity of our high-frequency search is markedly lower than in the low-frequency search. This is because here we have a shorter coherent integration time, a looser grid, and a higher threshold.

VII. SEARCH RESULTS

A. PowerFlux results

The PowerFlux algorithm and Loosely Coherent method compute power estimates for gravitational waves in a given frequency band for a fixed set of templates. The template parameters include frequency, the first frequency derivative, and sky location. The power estimates are grouped using all parameters except frequency into a set of arrays, and each array is examined separately.

Since the search target is a rare monochromatic signal, it would contribute excess power to one of the frequency bins after demodulation. The upper limit on the maximum excess relative to the nearby power values can then be established. For this analysis, we use a Universal statistic [34] that places conservative 95% C.L. upper limits for an arbitrary statistical distribution of noise power. The implementation of the Universal statistic used in this search has been tuned to provide close-to-optimal values in the common case of Gaussian distribution.

The upper limits obtained in the search are shown in Fig. 1. The numerical data for this plot can be obtained separately [39]. The upper (yellow) curve shows the upper limits for a worst-case (linear) polarization when the smallest amount of gravitational energy is projected toward Earth. The lower curve shows upper limits for an optimally oriented source. Because of the day-night variability of the interferometer sensitivity due to anthropogenic noise, the upper limits for linearly polarized sources are more severely affected by detector artifacts, as the detector response to linearly polarized sources varies with the same period. We are able to establish upper limits over the entire frequency range, including bands containing harmonics of 60 Hz and violin modes.

Each point in Fig. 1 represents a maximum over the sky; only small portions of the sky are excluded, near the ecliptic poles, which are highly susceptible to detector artifacts due to stationary frequency evolution produced by the combination of frequency derivative and Doppler shifts. The exclusion procedure is described in Ref. [19] and applied to 0.1% of the sky over the entire run.

If one assumes that the source spin down is solely due to the emission of gravitational waves, then it is possible to recast upper limits on source amplitude as a limit on source

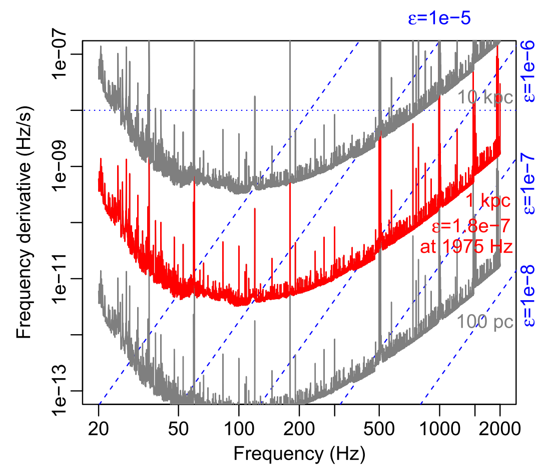

FIG. 8. Range of the PowerFlux search for neutron stars spinning down solely due to gravitational radiation. This is a superposition of two contour plots. The gray and red solid lines are contours of the maximum distance at which a neutron star could be detected as a function of gravitational-wave frequency f and its derivative $\dot{f}$. The dashed lines are contours of the corresponding ellipticity $\epsilon(f, \dot{f})$. The fine dotted line marks the maximum spin down searched. Together, these quantities tell us the maximum range of the search in terms of various populations (see the text for details).

ellipticity. Figure 8 shows the reach of our search under different assumptions on source distance. Superimposed are lines corresponding to sources of different ellipticities.

The detection pipeline produced 31 outliers located in the 1000–1033 Hz region heavily contaminated with violin modes (Table VIII), 134 outliers spanning only one data segment (about 1 month) that are particularly susceptible to detector artifacts (Tables VI and VII), and 48 outliers (Table V) that do not fall into either of those two categories. Each outlier is identified by a numerical index. We report the SNR, frequency, spin down, and sky location.

The "Segment" column describes the persistence of the outlier through the data and specifies which contiguous subset of the three equal partitions of the time span contributed most significantly to the outlier; see Ref. [25] for details. A true continuous signal from an isolated source would normally have [0,2] in this column (similar contribution from all three segments) or on rare occasions [0,1] or [1,2]. Any other range is indicative of a statistical fluctuation, an artifact, or a signal that does not conform to the phase evolution of Eq. (2).

During the O1 run, several simulated pulsar signals were injected into the data by applying a small force to the interferometer mirrors with auxiliary lasers. Several outliers were due to such hardware injections (Table II).

The recovery of the hardware injections gives us additional confidence that no potential signal was missed. Manual follow-up has shown noninjection outliers spanning all three segments to be caused by pronounced detector artifacts. Outlier number 72 in Table V spanning two segments was

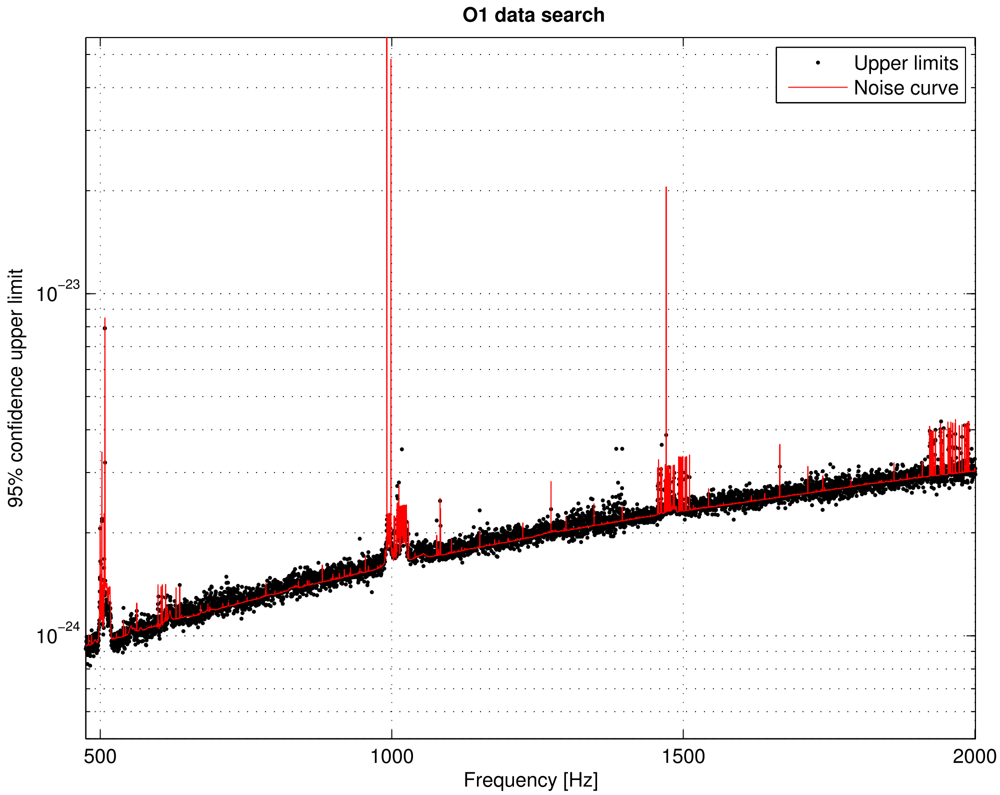

FIG. 9. Time-Domain $\mathcal{F}$-statistic pipeline O1 upper limits. Black dots are the 95% confidence upper limits for each frequency, and the red line denotes the H1 and L1 detectors' average noise curve rescaled by the factor $38/\sqrt{T_0}$, where $T_0 = 172328$ s is the observational time of the 2-sidereal-day time series segment. The factor of 38 is larger than the factor of 27.5 obtained in the low-frequency search, indicating loss of sensitivity due to a looser grid of templates used here.

TABLE II. Parameters of the hardware-injected simulated continuous-wave signals during the O1 data run (epoch GPS 1130529362). Because the interferometer configurations were largely frozen in a preliminary state after the first discovery of gravitational waves from a binary black hole merger, the hardware injections were not applied consistently. There were no injections in the H1 interferometer initially, and the initial injections in the L1 interferometer used an actuation method with significant inaccuracies at high frequencies. Right ascension (RA) and declination (DEC) are specified using J2000 epoch.

Label	Frequency (Hz)	Spin down (nHz/s)	RA_{J2000} (deg)	DEC_{J2000} (deg)
ip0	265.575533	-4.15×10^{-3}	71.55193	−56.21749
ip1	848.969641	-3.00×10^{-1}	37.39385	−29.45246
ip2	575.163521	-1.37×10^{-4}	215.25617	3.44399
ip3	108.857159	-1.46×10^{-8}	178.37257	−33.4366
ip4	1393.540559	-2.54×10^{-1}	279.98768	−12.4666
ip5	52.808324	-4.03×10^{-9}	302.62664	−83.83914
ip6	146.169370	-6.73×10^{0}	358.75095	−65.42262
ip7	1220.555270	-1.12×10^{0}	223.42562	−20.45063
ip8	191.031272	-8.65×10^{0}	351.38958	−33.41852
ip9	763.847316	-1.45×10^{-8}	198.88558	75.68959
ip10	26.341917	-8.50×10^{-2}	221.55565	42.87730
ip11	31.424758	-5.07×10^{-4}	285.09733	−58.27209
ip12	38.477939	-6.25×10^{0}	331.85267	−16.97288
ip13	12.428001	-1.00×10^{-2}	14.32394	−14.32394
ip14	1991.092401	-1.00×10^{-3}	300.80284	−14.32394

also investigated with a fully coherent follow-up based on the Einstein@Home pipeline [30,32]. No outlier was found to be consistent with the astrophysical signal model.

B. SkyHough results

In this section, we report the main results of the O1 all-sky search between 475 and 2000 Hz using the SkyHough pipeline, as described in Sec. V. In total, 71 0.1 Hz bands contained coincidence candidates: 19 in the 475–1200 Hz band, analyzed with higher sky resolution, and 52 in the 1200–2000 Hz band, analyzed with lower sky resolution.

After discarding all the clusters containing only one coincidence pair, this list was reduced to 25 outliers, 17 in the low-frequency band and 8 in the high-frequency band, which were further inspected. A detailed list of these remaining outliers is shown in Table IX. Among the 25 outliers, 17 were related to known line artifacts contaminating either H1 or L1 data, and 7 were identified with the hardware-injected pulsars ip1, ip2, ip7, and ip9.

Table III presents the parameters of the center of the clusters obtained related to these hardware injections. Two hardware injection were not recovered. Ip4 was not found since its spin-down was outside the search range, and ip14 was linearly polarized and had a strain amplitude h_0 below our sensitivity.

TABLE III. SkyHough hardware injection cluster information. The table provides the frequency, spin-down, and sky location of the cluster center related to each of the hardware injections found by the SkyHough search. In parentheses, the distance from the cluster center to the injected values are shown. Frequencies are converted to epoch GPS 1125972653.

Label	s_{mean}	Frequency (Hz)	Spin-down (nHz/s)	α (deg)	δ (deg)
ip2	30.50	575.1635 (0.0001)	0.0170 (0.0171)	215.1005 (0.1557)	3.0138 (0.4302)
ip9	35.85	763.8507 (0.0034)	−0.5567 (0.5567)	203.8965 (5.0109)	73.8445 (1.8451)
ip1	36.06	848.9657 (0.0053)	0.5497 (0.2497)	37.7549 (0.3611)	−25.2883 (4.1642)
ip7	41.61	1220.5554 (0.0009)	0.5482 (0.5718)	229.2338 (5.8082)	4.1538 (24.6044)

The only unexplained outlier around 715.7250 Hz, corresponding to Idx $= 6$ in Table IX, was further investigated. A multidetector Hough search was performed to verify the consistency of a possible signal. In this case, the maximum combined significance obtained was 5.98, while we would have expected a minimum value of 8.21 in case of a real signal. The outlier was also followed up with the Einstein@Home pipeline [32] using coherent integration times of 210 and 500 hr. This search covered signal frequencies in the range [715.724, 715.726] Hz (epoch GPS 1125972653), frequency derivatives over $[-2.2, -1.9] \times 10^{-9}$ Hz/s, and a sky region RA $= 1.063 \pm 0.020$ rad, DEC $= -0.205 \pm 0.020$ rad that included the whole associated cluster. This search showed that this candidate was not interesting and had a very low probability of having astrophysical origin.

Therefore, this SkyHough search did not find any evidence of a continuous gravitational-wave signal. Upper limits have been computed in each 0.1 Hz band, except for the 25 bands in which outliers were found.

C. Time-domain $\mathcal{F}$-statistic results

In the [475, 2000] Hz bandwidth range under study, 6300 0.25 Hz wide bands were analyzed. Vetoing candidates around the known interference lines, a certain fraction of the bandwidth was not analyzed. As a result 26% of the [475, 2000] Hz band was vetoed, overall.

Of 6300 bands analyzed, 307 bands were completely vetoed because of the line artifacts. As a result, the search was performed in the remaining 5993 bands. As 20 2-day segments have been chosen for the analysis, the 119,860 data segments were analyzed coherently with the $\mathcal{F}$-statistic. From the coherent search, we obtained around 8.6×10^{10} candidates. These candidates were subject to a search for initial coincidences in the second stage of the *Time-Domain $\mathcal{F}$-statistic* analysis. The search for coincidences was performed in all the bands except for the above-mentioned 307 that were completely vetoed. In the coincidence analysis, for each band, the coincidences among the candidates were searched in 20 2-day-long time frames. In Fig. 10, the results of the coincidence search are presented. The top panel shows the maximum coincidence multiplicity for each of the bands analyzed. The maximum multiplicity is an integer that varies from 3 to 20 because we require coincidence multiplicity of at least 3, and 20 is the number of time frames analyzed.

The bottom panel of Fig. 10 shows the results for the false alarm probability of coincidence for the coincidence with the maximum multiplicity. This false alarm probability is calculated using the formula from the Appendix of Ref. [27].

We define outliers as those coincidences with false alarm probabilities less than 0.1% This criterion was adopted in our Virgo data search [27] and also in one of the Einstein@Home searches [15]. From the analysis, we have excluded bands highly perturbed by violin modes and their harmonics. Thus, the following four bands were vetoed: [500, 509], [1001, 1025], [1483, 1511], and [1957, 1966] Hz. As a result, we obtained 74 outliers. The parameters of these outliers are listed in Table X. The parameters of a given coincidence are calculated as the mean values of the parameters of the candidates that enter a given coincidence. Among the 74 outliers, 10 are identified with the hardware injections. Table IV presents the estimated parameters obtained for these hardware injections, along with the absolute errors of the reconstructed parameters (the differences with respect to the injected parameters). The remaining 64 outliers include 10 that are seen only in H1 data and 1 that is in only the L1 data. Three of the outliers are absent in the last one-third of the data; one is

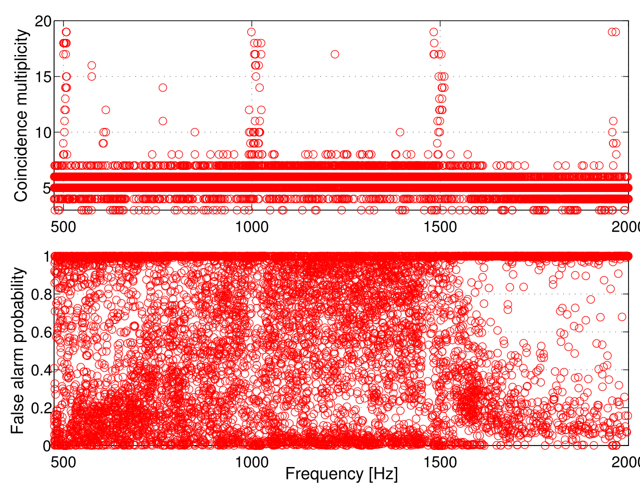

FIG. 10. Results of Time-Domain $\mathcal{F}$-statistic pipeline coincidences as a function of the band frequency. Top panel: maximum coincidence multiplicity. Bottom panel: false alarm probability for the coincidence with the maximum multiplicity.

TABLE IV. Hardware injection recovery with the Time-Domain $\mathcal{F}$-statistic pipeline. The values in parentheses are the absolute errors, that is, the difference with respect to the injection parameters. Frequencies are converted to epoch GPS 1131082120. The columns provide outliers false alarm probability (FAP) as well as the nominal frequencies and frequency derivatives, right ascensions and declinations. False alarm probability below code precision is displayed as 0.

Label	FAP	Frequency (Hz)	Spin-down (nHz/s)	α (deg)	δ (deg)
ip1	0	848.9687 (0.0007)	−2.4474 (2.1474)	39.4542 (2.0603)	−39.4354 (9.9830)
ip2	0	575.1638 (0.0003)	0.0162 (0.0163)	203.8658 (11.3903)	−27.1485 (30.5924)
ip4	0	1393.5286 (0.0021)	−24.901 (0.5991)	281.4735 (1.4858)	−13.3001 (0.8340)[a]
ip7	0	1220.5540 (0.0007)	−0.0784 (−1.0416)	218.8902 (4.5354)	−32.1127 (11.6621)
ip9	0	763.8472 (0.0001)	−0.0503 (0.0503)	197.8817 (1.0039)	75.9108 (0.2212)

[a]Spin-down of ip4 was outside the search range. The estimate was obtained by extending the spin-down range in the band where the hardware injection was located.

present in the first one-third of the data, and two have a wandering frequency that increases in the first one-third of the run, is constant in the second one-third, decreases in the last one-third of the run. The remaining 47 outliers seem to be harmonics of the same interference in the data. The distribution of the $\mathcal{F}$-statistic in a given time frame has approximately the same morphology for all the harmonics. The outliers are present both in H1 and L1 but not always in coincidence. When they are present in both detectors, their SNRs are not consistent and are at times much louder in L1. Moreover, the outliers appear in the stretch of a 2-day data segment where 87% of data are zeros. The remaining data in that segment are mainly a noise free modulated periodic signal. We conclude that the interference originates from the detectors themselves as it clearly appears in a stretch of data with a small fraction of science data. Consequently, no credible gravitational-wave candidates were found.

VIII. CONCLUSIONS

We have performed the most sensitive all-sky search to date for continuous gravitational waves in the range 475–2000 Hz using three different methods. We explored both positive and negative spin-downs and placed upper limits on expected and unexpected sources. Figure 1 shows a summary of the strain amplitude upper limits obtained for the three pipelines. One pipeline (PowerFlux) presents strict all-sky limits for circular-polarization and linear-polarization sources. The other two pipelines (SkyHough and Time-Domain $\mathcal{F}$-statistic) present frequentist population-averaged limits over the full sky and source polarization.

Outliers from the initial stages of each search method were meticulously followed up, but no candidates from any search survived scrutiny.

The use of the Universal statistic and Loosely Coherent algorithms allowed us to establish upper limits and achieve good detection efficiency (relative to the upper limit) in all frequency ranges, including highly contaminated areas.

The SkyHough pipeline added a viewpoint of robust Hough algorithm. Although the decrease in the sky grid resolution at 1200 Hz, tuned to reduce computational load, produced a jump in sensitivity of about 20%, this method offers an independent check of the other results. Future searches will use longer SFT time duration to allow the attainment of sensitivity close to PowerFlux at a reduced computational cost.

The use of a shorter coherence time and a looser grid for Time-Domain $\mathcal{F}$-statistic pipeline in the high-frequency search with respect to the low-frequency search resulted in loss of sensitivity by a factor of 3. With an increasing available computing power, the search of the next data set will be performed with a considerably longer coherent time that should result in a sensitivity slightly better than the worst case for the PowerFlux analysis.

At the highest frequencies, we are sensitive to neutron stars with an equatorial ellipticity as small as 1.8×10^{-7} and as far away as 1 kpc for favorable spin orientations. The maximum ellipticity a neutron star can theoretically support is at least 1×10^{-5} according to Refs. [55,56]. Our results exclude such maximally deformed pulsars above a 200 Hz stellar rotation frequency (400 Hz gravitational frequency) within 1 kpc. These upper limits improve upon those previously obtained from initial LIGO and Virgo data sets. The overall improvements in strain sensitivity come primarily from the improved noise floors of the Advanced LIGO interferometers over previous LIGO and Virgo interferometers, with reductions in upper limits of about a factor of 3 at frequencies above 100 Hz and larger reductions at lower frequencies.

Because these results exclude only maximal deformations in a limited distance range for higher frequencies, they do not permit firm conclusions about the equation of state determining neutron star structure. In future data taking, however, as detector sensitivities improve and longer data sets become available, the Galactic volume and bandwidth over which large deformations can be tested will expand to include many star-forming regions not currently accessible.

ACKNOWLEDGMENTS

The authors gratefully acknowledge the support of the United States National Science Foundation (NSF) for the construction and operation of the LIGO Laboratory and Advanced LIGO as well as the Science and Technology

Facilities Council (STFC) of the United Kingdom, the Max-Planck-Society (MPS), and the State of Niedersachsen/Germany for support of the construction of Advanced LIGO and construction and operation of the GEO600 detector. Additional support for Advanced LIGO was provided by the Australian Research Council. The authors gratefully acknowledge the Italian Istituto Nazionale di Fisica Nucleare (INFN), the French Centre National de la Recherche Scientifique (CNRS), and the Foundation for Fundamental Research on Matter supported by the Netherlands Organisation for Scientific Research for the construction and operation of the Virgo detector and the creation and support of the European Gravitational Observatory consortium. The authors also gratefully acknowledge research support from these agencies as well as by the Council of Scientific and Industrial Research of India, the Department of Science and Technology, India; the Science and Engineering Research Board (SERB), India; the Ministry of Human Resource Development, India; the Spanish Agencia Estatal de Investigación; the Vicepresidència i Conselleria d'Innovació; Recerca i Turisme and the Conselleria d'Educació i Universitat del Govern de les Illes Balears; the Conselleria d'Educació, Investigació, Cultura i Esport de la Generalitat Valenciana; the National Science Centre of Poland; the Swiss National Science Foundation (SNSF); the Russian Foundation for Basic Research; the Russian Science Foundation; the European Commission; the European Regional Development Funds (ERDF) the Royal Society; the Scottish Funding Council; the Scottish Universities Physics Alliance; the Hungarian Scientific Research Fund (OTKA); the Lyon Institute of Origins (LIO); the Paris Île-de-France Region; the National Research, Development and Innovation Office Hungary (NKFI); the National Research Foundation of Korea; Industry Canada and the Province of Ontario through the Ministry of Economic Development and Innovation; the Natural Science and Engineering Research Council Canada; the Canadian Institute for Advanced Research; the Brazilian Ministry of Science, Technology, Innovations, and Communications; the International Center for Theoretical Physics South American Institute for Fundamental Research (ICTP-SAIFR); the Research Grants Council of Hong Kong; the National Natural Science Foundation of China (NSFC); the Leverhulme Trust; the Research Corporation; the Ministry of Science and Technology (MOST), Taiwan; and the Kavli Foundation. The authors gratefully acknowledge the support of the NSF, STFC, MPS, INFN, CNRS, PL-Grid, and the State of Niedersachsen/Germany for provision of computational resources.

APPENDIX: OUTLIER TABLES

PowerFlux outliers passing all stages of automated follow-up from the 475–2000 Hz band are separated into four tables. Table V shows all outliers spanning two or more segments and outside the heavily contaminated frequency range 1000–1033 Hz. Table VIII shows outliers inside the contaminated region 1000–1033 Hz. Lastly, Tables VI and VII show "short" outliers using only one segment (approximately a month) of data. Table VI shows such short outliers below 1100 Hz, while Table VII lists short outliers above 1100 Hz. The splitting frequency of 1100 Hz was chosen only to put similar numbers of outliers in each table.

Table IX shows the parameters of the final 25 outliers from the SkyHough pipeline, along with comments on their likely origin. None of these outliers shows evidence of being a credible gravitational-wave signal.

Table X presents the parameters of the final 74 outliers from the Time-Domain $\mathcal{F}$-statistic pipeline, along with comments on their likely causes. None is a credible gravitational-wave signal.

TABLE V. Outliers that passed the PowerFlux detection pipeline spanning more than one segment and excluding the 1000–1033 Hz region heavily contaminated with violin modes. Only the highest-SNR outlier is shown for each 0.1 Hz frequency region. Outliers marked with "line" had strong narrow band disturbances identified near the outlier location. The "Segment" column reports the set of contiguous segments of the data that produced the outlier, as described in Sec. VII. Frequencies are converted to epoch GPS 1130529362.

Idx	SNR	Segment	Frequency (Hz)	Spin-down (nHz/s)	$\mathrm{RA}_{\mathrm{J2000}}$ (deg)	$\mathrm{DEC}_{\mathrm{J2000}}$ (deg)	Description
3	3886	[0, 2]	1220.55536	−0.300	229.053	−2.107	Injection 7, very different H1 and L1 sensitivities
4	456	[1, 2]	848.97002	−0.350	37.141	−29.612	Injection 1, L1 much more sensitive than H1
5	375	[1, 2]	763.84713	0.000	198.171	75.664	Injection 9, loud enough to be visible in background of H1 and L1
6	286	[0, 2]	575.16361	0.000	215.370	3.558	Injection 2, L1 more sensitive than H1
14	126	[0, 1]	1080.00097	0.200	271.159	66.681	Exceptionally strong coincident bin-centered lines at 1080 Hz
16	85	[0, 2]	1487.98795	−9.550	144.132	−66.819	Strong bin-centered line in H1 at 1488.00 Hz

(Table continued)

TABLE V. *(Continued)*

Idx	SNR	Segment	Frequency (Hz)	Spin-down (nHz/s)	RA_{J2000} (deg)	DEC_{J2000} (deg)	Description
19	68	[0, 2]	1220.43752	−1.975	169.199	−0.960	Induced by injection 7
24	41	[1, 2]	767.96349	1.475	118.599	78.067	Strong bin-centered line in H1 at 768 Hz
25	37	[1, 2]	615.00752	−4.700	202.130	63.562	Strong broad line in L1
26	37	[0, 1]	713.38012	−3.900	223.547	64.304	Strong bin-centered line in L1 at 713.400 Hz
27	36	[1, 2]	585.38340	−9.550	207.405	0.724	Strong bin-centered line in L1 at 585.400 Hz
31	29	[0, 2]	1220.46981	−7.650	177.333	53.647	Induced by injection 7
32	29	[0, 1]	943.98085	1.250	341.520	70.413	Strong bin-centered line in H1 at 944.00 Hz
33	28	[0, 2]	910.06257	1.475	100.432	80.276	Strong broad line in H1
34	27	[0, 1]	980.41316	0.425	68.498	19.939	Strong bin-centered line in L1 at 980.500 Hz, line in H1
35	26	[0, 1]	1457.59127	0.900	5.161	22.809	Highly nonstationary L1 data
36	26	[0, 2]	767.97611	−4.025	106.321	−57.243	Bin-centered line in H1 at 768.00 Hz
37	26	[0, 2]	1255.99635	−1.725	100.106	−67.630	Line in H1 at 1256 Hz
40	23	[1, 2]	1456.03964	−1.600	215.391	−69.386	Highly nonstationary H1 data, line at 1456.00 Hz
41	23	[0, 1]	2000.00108	−4.275	146.821	−64.950	Line in H1, violin mode harmonic region
42	23	[0, 1]	831.94019	−7.550	139.056	−28.186	Bin-centered line in H1 at 832.00 Hz
43	22	[0, 1]	918.82255	−1.525	294.016	−66.661	Strong broad line in L1
44	21	[0, 2]	899.29679	1.475	298.627	26.700	Strong broad line in H1
45	21	[1, 2]	968.29014	−7.550	105.510	−69.138	Mismatch in SNR between H1 and L1
46	21	[0, 1]	943.94642	−6.450	72.434	−43.175	Bin-centered line in H1 at 944.00 Hz
47	20	[0, 2]	1167.94911	1.325	81.001	−36.869	Bin-centered line in H1 at 1168.00 Hz
48	20	[0, 1]	1983.05344	−4.350	28.614	−29.172	Line in L1 at 1983.0994 Hz
49	20	[0, 2]	1393.47837	−0.075	269.418	−38.074	Appears to be associated with injection 4
50	20	[1, 2]	559.75418	−4.975	99.663	2.943	Bin-centered line in L1 at 559.800 Hz
51	18	[0, 1]	1471.00891	−0.600	19.261	82.386	Highly nonstationary H1 spectrum
52	18	[1, 2]	629.87432	−4.025	208.388	61.733	Strong broad line in L1
53	17	[0, 1]	918.73177	1.325	77.766	−40.562	Strong broad line in L1
54	17	[1, 2]	623.96957	−0.075	198.261	63.320	Bin-centered line in H1 at 624.00 Hz
55	17	[1, 2]	588.29660	−2.325	20.174	63.144	Strong bin-centered line in L1 at 588.300 Hz
57	17	[0, 1]	1455.93002	−1.075	72.852	−37.095	Very nonstationary H1 spectrum, line at 1456.00 Hz
58	17	[0, 1]	567.99073	0.525	275.690	77.944	Strange coincident lines at 568.00 Hz
59	16	[1, 2]	906.51613	−5.650	114.204	7.807	Bin-centered line in L1 at 906.600 Hz
60	16	[0, 2]	588.31398	−5.550	208.182	−49.133	Strong bin-centered line in L1 at 588.300 Hz
62	16	[0, 1]	1400.00418	0.675	85.821	−67.453	Bin-centered line in H1 at 1400.00 Hz
63	16	[0, 2]	575.09743	−10.525	223.480	54.438	Induced by injection 2
64	15	[1, 2]	1055.67464	−8.850	52.210	−62.000	Poor coherence between H1 and L1
65	15	[0, 2]	918.75333	−4.250	259.272	65.613	Strong broad line in L1
66	14	[0, 1]	600.00424	−5.950	194.962	−83.060	Strong line in H1 near 600 Hz
67	14	[0, 1]	906.72776	−4.475	95.914	8.234	Strong broad line in H1
68	13	[1, 2]	1198.55097	1.175	197.933	80.202	Strong broad line in H1
69	13	[0, 2]	627.89160	−8.200	225.017	32.253	Bin-centered line in L1 at 627.900 Hz
71	12	[1, 2]	966.05168	−5.725	290.296	45.961	H1 and L1 SNR inconsistent
72	12	[0, 1]	956.52184	−5.950	96.516	6.398	

TABLE VI. Outliers below 1100 Hz that passed the PowerFlux detection pipeline spanning only one segment, excluding the 1000–1033 Hz region heavily contaminated with violin modes. Only the highest-SNR outlier is shown for each 0.1 Hz frequency region. The "Segment" column reports the set of contiguous segments of the data that produced the outlier, as described in Sec. VII. Frequencies are converted to epoch GPS 1130529362.

Idx	SNR	Segment	Frequency (Hz)	Spin-down (nHz/s)	RA_{J2000} (deg)	DEC_{J2000} (deg)
73	122634	[0, 0]	998.67165	−6.050	34.496	−58.000
74	76138	[0, 0]	998.61134	1.175	50.986	18.219
78	485	[2, 2]	512.01668	−3.425	22.826	−88.770
83	69	[1, 1]	832.01071	−6.600	178.258	−75.767
84	61	[1, 1]	863.96498	−7.225	207.792	54.356
86	52	[1, 1]	952.02462	−4.200	156.420	−86.793
87	48	[1, 1]	781.48875	−9.175	227.909	39.730
89	44	[1, 1]	1079.93838	−6.050	185.624	58.142
96	28	[0, 0]	1099.69279	−9.500	62.525	−17.371
97	28	[2, 2]	918.70042	−5.975	135.889	−27.388
102	25	[0, 0]	945.25946	−4.425	105.182	−2.896
108	20	[1, 1]	568.53389	−5.075	270.104	−61.403
109	20	[2, 2]	1080.11043	−7.325	307.143	−1.254
110	19	[2, 2]	824.02132	−5.700	147.900	−86.736
111	19	[0, 0]	899.25908	−5.650	337.827	−21.074
113	19	[2, 2]	990.04856	0.300	135.434	−26.528
114	19	[2, 2]	716.23123	−0.075	168.445	20.834
115	19	[1, 1]	568.01764	−2.225	251.325	−89.632
116	19	[1, 1]	1096.02101	−4.450	133.692	−83.005
117	19	[0, 0]	922.55918	−0.450	64.475	4.328
119	18	[2, 2]	1088.01257	−10.825	248.325	39.022
121	18	[2, 2]	900.87618	−4.750	308.565	23.094
122	18	[2, 2]	900.73436	−5.900	161.021	−19.505
123	17	[2, 2]	523.61892	−6.825	240.077	−55.972
124	17	[1, 1]	475.32726	−6.025	207.149	78.036
126	17	[1, 1]	1088.04594	0.325	18.340	−52.698
129	17	[1, 1]	1095.98516	−10.525	159.987	−62.138
130	17	[1, 1]	475.36243	−8.625	283.160	−83.890
131	16	[2, 2]	625.01993	−5.925	333.353	50.108
132	16	[0, 0]	912.06903	−2.325	281.739	−53.318
133	16	[2, 2]	716.37292	−8.400	306.163	12.283
134	16	[2, 2]	1091.97016	−5.475	257.005	−45.295
135	16	[0, 0]	922.66069	1.400	4.635	−37.224
137	16	[1, 1]	1085.88189	−3.275	222.923	41.844
138	16	[1, 1]	799.61576	−4.225	305.876	58.952
141	16	[1, 1]	945.43339	−4.575	277.653	−1.384
143	16	[0, 0]	1063.98385	−0.450	89.302	−58.822
144	16	[2, 2]	874.92611	−5.900	198.168	36.620
147	16	[2, 2]	1080.26045	−5.425	147.600	−21.563
148	16	[2, 2]	991.13399	−9.700	217.041	21.846
149	16	[1, 1]	920.03446	−5.200	309.442	−84.932
152	15	[0, 0]	943.20137	−8.275	60.640	−34.099
153	15	[1, 1]	971.53220	−1.200	270.236	33.046
154	15	[2, 2]	900.74745	−7.825	165.665	−30.418
156	15	[1, 1]	945.41047	−10.600	260.757	3.250

(Table continued)

TABLE VI. *(Continued)*

Idx	SNR	Segment	Frequency (Hz)	Spin-down (nHz/s)	RA_{J2000} (deg)	DEC_{J2000} (deg)
159	15	[2, 2]	700.07700	−1.325	143.438	53.430
160	15	[1, 1]	961.40660	−8.400	318.893	27.718
161	15	[1, 1]	1054.71444	−9.800	0.704	−4.956
165	14	[2, 2]	831.64901	−3.125	194.537	−39.518
173	14	[1, 1]	739.29278	−0.600	318.296	−43.429
176	14	[0, 0]	718.00248	−5.675	213.134	−49.747
178	14	[1, 1]	669.61556	−1.100	57.094	−34.323
179	14	[0, 0]	775.14530	−8.450	244.756	−52.288
181	14	[0, 0]	1039.11823	−1.375	313.591	35.538
182	14	[2, 2]	754.30629	−5.450	16.599	47.778
183	14	[1, 1]	633.73616	−10.900	11.121	−54.400
192	13	[1, 1]	1069.18221	−4.850	136.156	−16.451
196	13	[1, 1]	583.96498	−9.500	311.580	41.127
206	13	[2, 2]	758.50361	−2.400	136.803	−35.273
207	13	[0, 0]	1087.96981	−9.250	54.309	−60.667
209	12	[2, 2]	662.79818	−5.200	219.379	35.883
211	12	[0, 0]	895.31856	−9.575	242.924	15.227

TABLE VII. Outliers above 1100 Hz that passed the PowerFlux detection pipeline spanning only one segment. Only the highest-SNR outlier is shown for each 0.1 Hz frequency region. The “Segment” column reports the set of contiguous segments of the data that produced the outlier, as described in Sec. VII. Frequencies are converted to epoch GPS 1130529362.

Idx	SNR	Segment	Frequency (Hz)	Spin-down (nHz/s)	RA_{J2000} (deg)	DEC_{J2000} (deg)
75	5854	[0, 0]	1456.14766	−0.175	136.769	−41.785
76	2713	[1, 1]	1987.38812	−8.100	115.653	−70.974
80	105	[1, 1]	1824.00927	−8.250	126.515	−75.314
81	91	[2, 2]	1393.56417	−10.075	318.820	−10.426
82	72	[0, 0]	1327.89729	−7.325	140.109	69.425
85	59	[1, 1]	1872.06302	−7.600	348.724	−87.309
88	44	[0, 0]	1135.96045	−7.525	218.121	64.723
90	41	[1, 1]	1997.31629	−6.175	61.621	−65.686
91	37	[0, 0]	1369.76707	−0.050	187.539	59.193
92	36	[0, 0]	1999.90597	0.750	20.310	70.095
95	31	[0, 0]	1690.86031	−2.875	96.307	−14.940
98	27	[0, 0]	1999.78615	−5.300	81.182	32.271
99	27	[1, 1]	1247.54194	−6.900	128.268	−45.602
103	25	[0, 0]	1999.83424	−0.450	61.487	47.583
104	23	[1, 1]	1446.70535	−7.725	22.583	−68.576
105	21	[2, 2]	1393.29262	−8.600	168.938	24.362
106	21	[0, 0]	1372.62964	−3.400	89.257	−41.198
107	20	[0, 0]	1135.90451	−9.050	118.203	−25.813
112	19	[2, 2]	1393.44556	−10.300	179.179	−86.352
120	18	[1, 1]	1262.53007	−1.025	132.290	−51.838
125	17	[1, 1]	1213.68816	−7.975	347.921	41.708
127	17	[1, 1]	1290.46538	−2.250	56.528	−56.177
128	17	[1, 1]	1463.16241	−3.050	34.883	37.388
136	16	[1, 1]	1424.20719	−10.250	143.258	54.532

(Table continued)

TABLE VII. *(Continued)*

Idx	SNR	Segment	Frequency (Hz)	Spin-down (nHz/s)	RA_{J2000} (deg)	DEC_{J2000} (deg)
139	16	[1, 1]	1335.54724	0.000	27.733	−76.368
140	16	[0, 0]	1213.56733	−4.925	104.723	66.604
142	16	[1, 1]	1276.81304	−7.075	58.235	−29.473
145	16	[0, 0]	1907.05681	−5.250	272.503	−46.509
146	16	[2, 2]	1528.32712	−4.950	37.441	−60.096
150	15	[1, 1]	1459.94901	−9.950	163.428	−22.664
151	15	[2, 2]	1401.51757	−7.250	355.062	−38.577
155	15	[1, 1]	1138.62182	−4.250	90.540	−33.848
157	15	[1, 1]	1256.01957	−9.275	176.253	−78.174
158	15	[1, 1]	1211.07792	−0.475	348.328	79.398
162	14	[1, 1]	1463.20594	−5.200	15.555	28.395
163	14	[0, 0]	1219.64849	0.050	179.645	−29.748
164	14	[2, 2]	1264.11240	−5.100	313.522	18.441
166	14	[2, 2]	1295.86238	−3.900	181.282	−55.826
167	14	[2, 2]	1395.17951	0.350	162.187	−56.606
168	14	[0, 0]	1264.56939	−3.875	260.820	23.151
169	14	[2, 2]	1288.87309	−1.900	337.759	−17.706
170	14	[2, 2]	1203.61330	−3.825	170.297	−17.434
171	14	[1, 1]	1368.72368	−2.875	153.808	−53.399
172	14	[1, 1]	1337.95543	−3.150	92.898	−48.705
174	14	[0, 0]	1405.16819	−2.050	358.179	−32.990
175	14	[1, 1]	1230.31634	0.800	205.853	25.811
177	14	[0, 0]	1352.50502	−8.400	294.685	−2.192
180	14	[2, 2]	1421.97637	−1.675	216.086	77.049
184	14	[1, 1]	1384.01262	−0.250	344.524	−69.144
185	14	[0, 0]	1251.71109	−0.375	88.753	47.800
186	14	[1, 1]	1180.70083	−0.575	74.681	−30.772
187	14	[2, 2]	1404.40200	−6.400	105.584	46.302
188	13	[0, 0]	1329.97102	−4.750	175.844	46.741
189	13	[2, 2]	1130.57326	−4.000	103.921	43.754
190	13	[1, 1]	1302.48986	−5.450	186.382	−59.427
191	13	[2, 2]	1248.31576	0.875	85.718	−10.040
193	13	[1, 1]	1107.06549	−6.450	127.799	−10.620
194	13	[2, 2]	1451.70229	−9.875	238.959	46.016
195	13	[1, 1]	1296.76012	−4.750	260.379	33.317
197	13	[0, 0]	1171.26882	−4.150	15.889	−37.954
198	13	[0, 0]	1165.20479	−4.825	60.686	−23.324
199	13	[1, 1]	1164.53396	−6.750	284.184	31.085
200	13	[1, 1]	1113.03840	−8.575	194.191	−63.810
201	13	[1, 1]	1266.40557	−9.275	359.080	18.866
202	13	[1, 1]	1177.23828	−6.950	302.299	65.853
203	13	[1, 1]	1285.67481	−2.750	346.041	−33.719
204	13	[1, 1]	1186.91571	−8.950	211.272	18.279
205	13	[0, 0]	1432.28413	−10.450	55.297	−35.353
208	13	[0, 0]	1132.56792	−6.625	248.673	37.290
210	12	[2, 2]	1257.08005	−0.850	117.394	−38.201
212	12	[1, 1]	1321.09437	−4.050	67.216	−35.597
213	12	[1, 1]	1324.20852	−7.150	104.807	56.301

TABLE VIII. PowerFlux outliers in the 1000–1033 Hz region heavily contaminated with violin modes. Only the highest SNR outlier is shown for each 0.1 Hz frequency region. Outliers marked with "line" had strong narrow band disturbances identified near the outlier location. The "Segment" column reports the set of contiguous segments of the data that produced the outlier, as described in Sec. VII. Frequencies are converted to epoch GPS 1130529362.

Idx	SNR	Segment	Frequency (Hz)	Spin-down (nHz/s)	RA_{J2000} (deg)	DEC_{J2000} (deg)	
1	20746	[1, 2]	1019.64700	−4.625	246.424	80.922	Extremely strong bin-centered line in L1
2	20438	[0, 1]	1020.36752	−1.750	253.492	63.937	Lines in H1 and L1
7	283	[0, 2]	1008.00325	−10.825	221.934	43.985	Very strong line in L1
8	264	[1, 2]	1008.12309	−8.600	301.450	−25.837	Very strong line in L1
9	257	[0, 1]	1007.92946	0.575	90.115	11.329	Very strong line in L1, line in H1 at different frequency
10	249	[1, 2]	1026.85819	−9.925	169.924	−66.143	Forest of strong lines in L1
11	185	[1, 2]	1023.86681	−5.350	314.269	−4.805	Forest of strong lines in L1
12	182	[1, 2]	1023.91746	1.250	153.699	75.645	Extremely strong line in L1
13	133	[0, 2]	1012.64960	−6.950	279.830	−18.978	Strong lines in L1, highly nonstationary spectrum, disturbed H1 spectrum
15	118	[1, 2]	1023.88441	−5.925	164.783	12.160	Forest of strong lines in L1
17	74	[0, 2]	1032.24361	−10.675	150.097	−53.175	Forest of strong lines in L1
18	72	[0, 2]	1026.77755	−10.250	104.093	−14.244	Forest of strong lines in L1
20	59	[0, 1]	1032.80017	−7.075	353.600	−66.276	Forest of strong lines in L1
21	53	[0, 2]	1031.18496	−9.875	157.882	−34.654	Forest of strong lines in L1
22	50	[0, 2]	1026.93116	−6.100	300.750	26.695	Forest of strong lines in L1
23	43	[0, 2]	1030.85351	−3.375	145.333	77.333	Forest of strong lines in L1
28	36	[0, 2]	1029.16420	−5.900	94.435	−68.285	Forest of strong lines in L1
29	32	[0, 1]	1006.53372	−5.550	212.656	−74.205	Strange broad line in H1
30	31	[0, 2]	1032.22826	−7.775	132.317	−45.682	Forest of strong lines in L1
38	24	[1, 2]	1026.10892	−2.450	29.852	−82.280	Forest of strong lines in L1
39	24	[1, 2]	1026.06630	−1.925	124.580	−66.716	Forest of strong lines in L1
56	17	[1, 2]	1016.00465	−4.900	107.871	4.395	Highly nonstationary L1 data
61	16	[0, 1]	1003.61312	−1.175	108.017	−37.989	Strong broad line in H1
70	13	[1, 2]	1006.00859	−6.325	112.936	5.218	Bin-centered line in L1 at 1006.100 Hz, broad line in H1
77	510	[0, 0]	1027.01297	1.025	26.276	70.439	
79	185	[1, 1]	1022.43734	−2.425	117.977	−56.277	
93	36	[1, 1]	1027.31427	0.550	155.955	65.509	
94	36	[0, 0]	1019.41689	−9.050	310.849	−53.911	
100	27	[0, 0]	1006.51372	−10.975	223.516	14.553	
101	27	[0, 0]	1005.90983	−4.925	270.705	72.119	
118	18	[0, 0]	1000.00868	−9.250	261.463	37.283	

TABLE IX. SkyHough pipeline outliers in the range of frequencies between 475 and 2000 Hz after the population veto. The table provides the frequency, spin-down, and sky location of the cluster centers found by the SkyHough search. $\#_{\mathrm{cluster}}$ is the size of the cluster in terms of number of coincident pairs, s_{max} and s_{mean} are the maximum and mean values of the cluster significance, $\#_{L1}$ and $\#_{H1}$ are the numbers of different candidates producing coincidence pairs from the different data sets, and s^*_{L1} and s^*_{H1} are the maximum significance values obtained by analyzing the data from H1 and L1 separately. Frequencies are converted to epoch GPS 1125972653.

Idx	Frequency (Hz)	α (rad)	δ (rad)	Spin-down (nHz/s)	s_{mean}	$\#_{\mathrm{cluster}}$	$\#_{\mathrm{L1}}$	$\#_{\mathrm{H1}}$	s^*_{L1}	s^*_{H1}	s_{max}	Description
1	501.6000	−1.4445	1.2596	0.9374	10.66	5	2	3	11.31	89.18	10.71	Quad violin mode 1st harmonic region (H1 & L1)
2	511.9968	−1.4218	1.2070	0.6773	16.31	4927	298	226	10.47	101.36	18.73	Quad violin mode 1st harmonic region (H1 & L1)
3	512.0027	1.7085	−1.1996	−0.6071	16.33	3007	245	246	11.20	101.55	18.85	Quad violin mode 1st harmonic region (H1 & L1)
4	568.0011	1.5942	−1.1783	−0.1839	7.18	3867	415	125	8.82	9.81	9.05	8 Hz comb (H1 & L1)
5	575.1635	−2.5290	0.0526	0.0170	30.50	1974	275	78	46.66	26.54	33.75	Hardware injection ip2
6	715.7250	1.0629	−0.2049	−2.0400	5.48	5	3	4	6.53	6.50	5.53	Unknown
8	763.8507	−2.7245	1.2888	−0.5567	35.85	6064	297	91	41.29	43.43	42.33	Hardware injection ip9
9	763.9016	−2.1715	0.9109	−7.1318	18.19	611	151	56	17.45	22.99	19.84	Hardware injection child ip9
11	824.0035	1.6679	−1.1996	−0.7762	7.56	1111	81	123	8.09	10.83	8.43	8 Hz comb (H1 & L1)
12	848.9657	0.6589	−0.4414	0.5497	36.06	5329	342	117	48.63	37.64	42.17	Hardware injection ip1
13	849.0020	0.4565	−0.6807	−4.0716	25.19	1983	331	108	31.08	29.57	29.35	Hardware injection child ip1
14	895.9988	−1.5481	1.1744	0.2368	10.33	244	35	79	6.48	69.62	11.45	8 Hz comb (H1 & L1)
15	952.0018	1.5957	−1.1797	−0.3216	18.57	4353	355	189	18.36	27.59	21.86	8 Hz comb (H1 & L1)
16	952.1017	−0.3965	−1.3294	−9.8134	9.08	416	138	62	9.17	15.29	9.98	8 Hz comb (H1 & L1)
17	1079.9981	−1.5517	1.1798	0.3367	22.98	2639	402	129	51.28	17.88	25.90	8 Hz comb (H1 & L1)
18	1080.0022	1.6073	−1.1825	−0.4562	22.95	5276	428	172	52.66	17.84	25.89	8 Hz comb (H1 & L1)
19	1080.1007	−0.2290	−1.3906	−9.9428	10.79	451	117	49	20.45	9.52	12.60	8 Hz comb (H1 & L1)
21	1220.5492	−2.2823	0.0725	0.5482	34.69	291	63	43	66.56	37.98	48.10	Hardware injection ip7
22	1220.7094	−1.6804	−0.5910	−9.6702	6.14	17	12	11	7.37	8.32	6.58	Hardware injection child ip7
44	1475.0997	1.5636	−1.1725	−0.0308	10.87	42	8	19	6.64	77.42	11.72	Quad violin mode 3rd harmonic region (H1 & L1)
45	1482.5000	−2.8976	1.0123	0.7317	9.04	2	1	2	6.58	51.78	9.05	Quad violin mode 3rd harmonic region (H1 & L1)
46	1487.8976	1.8780	1.1717	−1.7738	6.69	2	1	2	6.53	10.19	6.75	Quad violin mode 3rd harmonic region (H1)
66	1903.9302	−1.8796	1.5402	0.1383	15.51	65	28	12	35.47	39.89	35.48	8 Hz comb (H1 & L1)
67	1904.0020	1.5885	−1.1737	−0.4096	29.00	4779	340	141	34.94	40.65	36.82	8 Hz comb (H1 & L1)
68	1904.1028	0.9560	−1.3834	− 10.0406	15.11	925	194	51	16.36	24.82	19.12	8 Hz comb (H1 & L1)

TABLE X. Time-Domain $\mathcal{F}$-statistic pipeline outliers in the range of frequencies between 475 and 2000 Hz. The columns provide outliers false alarm probability (FAP) as well as the nominal frequencies and frequency derivatives, right ascensions and declinations found for the outliers, along with comments indicating the likely sources of the outliers. Outliers described as "harmonics of a detector interference" are harmonics of an interference present in the detectors data when no science data are taken.

Idx	FAP	Frequency (Hz)	Spin-down (nHz/s)	RA_{J2000} (deg)	DEC_{J2000} (deg)	Description
1	9.1×10^{-4}	476.23802	−1.613	314.9096	−70.2754	Harmonic of a detector interference
2	8.0×10^{-4}	486.89080	−0.061	304.1872	44.0319	Harmonic of a detector interference
3	5.3×10^{-4}	487.61370	−1.133	268.2052	30.6643	Absent in the last 1/3 of the data
4	8.3×10^{-4}	492.22690	−0.615	280.4806	20.3164	Harmonic of a detector interference
5	2.0×10^{-5}	499.26822	0.224	265.2608	70.6734	Present only in H1
6	3.3×10^{-7}	499.28018	−1.546	119.7586	−83.1059	Present only in H1
7	1.3×10^{-4}	518.14518	−0.251	320.7519	35.3491	Harmonic of a detector interference
8	1.3×10^{-4}	531.94696	0.251	287.7129	29.1385	Absent in the last 1/3 of the data
9	1.3×10^{-4}	571.66195	−1.235	350.9658	−72.5879	Harmonic of a detector interference
10	1.3×10^{-4}	575.16544	0.293	219.7073	12.2089	Injection 2
11	1.3×10^{-4}	575.16377	0.016	203.8658	−27.1485	Injection 2
12	5.9×10^{-4}	580.85725	0.104	31.4819	−66.8292	Harmonic of a detector interference
13	3.7×10^{-4}	593.93609	−0.340	195.5173	−85.6270	Harmonic of a detector interference
14	5.9×10^{-4}	603.61601	−2.460	253.8641	30.8522	Harmonic of a detector interference
15	2.7×10^{-4}	604.42590	−0.034	146.0965	25.3840	Present only in H1
16	2.8×10^{-4}	604.42583	−0.237	141.1892	4.7461	Present only in H1
17	3.9×10^{-7}	606.60486	−0.204	149.2635	26.6243	Present only in H1
18	1.3×10^{-5}	606.60513	−0.203	138.3114	1.3266	Present only in H1
19	5.4×10^{-4}	631.47115	−1.004	270.0083	43.2007	Absent in the last 1/3 of the data
20	1.9×10^{-4}	659.09677	−2.865	298.0274	−73.3156	Harmonic of a detector interference
21	9.9×10^{-4}	690.09526	−0.659	275.6423	32.2947	Harmonic of a detector interference
22	5.6×10^{-4}	735.36919	−0.679	66.2231	−82.7547	Harmonic of a detector interference
23	0	763.84721	0.050	197.8817	75.9108	Injection 9
24	0	763.86856	−4.532	166.7853	−65.5177	Injection 9
25	8.6×10^{-4}	769.53252	−2.470	329.3430	−80.4823	Harmonic of a detector interference
26	1.6×10^{-4}	787.45070	−0.803	298.4857	52.5868	Harmonic of a detector interference
27	1.2×10^{-4}	806.10968	−3.761	287.7636	−73.5434	Harmonic of a detector interference
28	5.0×10^{-4}	820.86500	−2.207	265.9691	40.4204	Harmonic of a detector interference
29	3.0×10^{-4}	820.86681	−0.189	48.1082	−81.1524	Harmonic of a detector interference
30	8.4×10^{-4}	831.52219	−0.389	52.4265	−81.1168	Harmonic of a detector interference
31	0	848.92226	−0.201	217.6862	26.1052	Injection 1
32	0	848.92781	−1.907	203.5355	−29.8588	Injection 1
33	4.0×10^{-5}	890.14676	−1.985	264.8075	30.4969	Harmonic of a detector interference
34	8.7×10^{-5}	912.66971	0.237	8.9448	−78.2029	Harmonic of a detector interference
35	8.7×10^{-6}	924.03645	−0.613	275.1312	51.0793	Harmonic of a detector interference
36	8.4×10^{-5}	952.61767	−0.479	50.3141	−73.5387	Harmonic of a detector interference
37	2.3×10^{-4}	992.81797	−0.514	281.6408	53.6023	Harmonic of a detector interference
38	1.2×10^{-6}	992.82278	−0.884	48.8682	−81.6560	Harmonic of a detector interference
39	1.7×10^{-5}	996.25027	0.239	271.2557	67.5053	Present only in H1
40	3.8×10^{-7}	996.25657	−1.660	111.3151	−76.5712	Present only in H1
41	3.8×10^{-4}	1000.81171	−1.333	92.7694	−85.8077	Harmonic of a detector interference
42	7.9×10^{-5}	1003.90928	0.242	274.4174	66.8185	Present only in H1
43	3.6×10^{-7}	1003.92034	−3.527	156.6592	−81.4408	Present only in H1
44	6.2×10^{-4}	1054.83208	−0.047	281.0917	46.6542	Harmonic of a detector interference
45	3.3×10^{-4}	1058.46127	−0.574	41.8203	−83.6738	Harmonic of a detector interference
46	2.7×10^{-4}	1142.02054	−1.289	18.8221	−85.2794	Harmonic of a detector interference
47	3.6×10^{-4}	1149.51676	−1.780	112.2596	−85.3719	Harmonic of a detector interference
48	4.0×10^{-4}	1163.07712	−0.461	71.0369	−77.8010	Harmonic of a detector interference
49	3.9×10^{-4}	1196.01380	−0.079	73.4466	−76.2717	Harmonic of a detector interference
50	3.6×10^{-4}	1201.09880	−0.391	75.8100	−76.7984	Harmonic of a detector interference
51	6.4×10^{-4}	1201.83843	−0.036	45.6877	−79.2300	Harmonic of a detector interference
52	3.0×10^{-4}	1210.30530	0.282	67.6575	−75.6512	Harmonic of a detector interference
53	0	1220.55246	−0.364	226.2481	−7.0719	Injection 7

(Table continued)

TABLE X. *(Continued)*

Idx	FAP	Frequency (Hz)	Spin-down (nHz/s)	RA_{J2000} (deg)	DEC_{J2000} (deg)	Description
54	0	1220.55400	−0.078	218.8902	−32.1127	Injection 7
55	8.3×10^{-4}	1224.35567	−1.593	269.1917	47.7573	Harmonic of a detector interference
56	4.7×10^{-4}	1250.03185	−0.632	58.5959	−81.8576	Harmonic of a detector interference
57	1.9×10^{-4}	1252.45409	−0.649	58.7640	−82.0590	Harmonic of a detector interference
58	2.3×10^{-4}	1253.19279	−0.946	276.3357	42.2750	Harmonic of a detector interference
59	6.8×10^{-4}	1287.31747	−0.692	81.6594	−77.4641	Harmonic of a detector interference
60	3.9×10^{-4}	1293.85609	−2.777	132.0928	−83.0378	Harmonic of a detector interference
61	6.5×10^{-5}	1310.08345	−2.338	113.5595	−82.3435	Harmonic of a detector interference
62	3.0×10^{-4}	1317.10722	−1.791	100.7620	−81.3209	Harmonic of a detector interference
63	1.1×10^{-4}	1381.05818	−0.239	279.5478	51.3271	Harmonic of a detector interference
64	4.3×10^{-4}	1383.22336	−2.009	108.8794	−81.2435	Harmonic of a detector interference
65	0	1393.54760	−2.011	323.8507	2.7705	Injection 4
66	0	1393.55069	−1.496	336.9224	−25.1755	Injection 4
67	4.0×10^{-4}	1411.31585	−2.444	115.2990	−80.9642	Harmonic of a detector interference
68	1.3×10^{-4}	1422.69979	−2.169	113.5662	−80.7357	Harmonic of a detector interference
69	8.3×10^{-4}	1468.11317	0.110	329.1319	−7.2537	Wandering frequency
70	8.3×10^{-4}	1468.11329	0.115	332.3289	−15.9424	Wandering frequency
71	2.4×10^{-4}	1573.10838	−0.908	78.8100	−79.5921	Harmonic of a detector interference
72	9.9×10^{-4}	1660.29579	−1.255	268.8632	52.7214	Harmonic of a detector interference
73	6.7×10^{-4}	1908.10543	−1.969	254.0502	−81.8658	Present in 1st 1/3 of the run
74	1.6×10^{-6}	1967.56836	−1.891	102.5901	−70.5698	Present only in L1

[1] J. Aasi *et al.* (LIGO Scientific Collaborations), Advanced LIGO, Classical Quantum Gravity **32**, 7 (2015).

[2] P. Lasky, Gravitational waves from neutron stars: A review, Pub. Astron. Soc. Aust. **32**, e034 (2015).

[3] K. Glampedakis and L. Gualtieri, chapter in "Physics and Astrophysics of Neutron Stars", NewCompStar COST Action 1304 (2017), http://www.cost.eu/.

[4] B. P. Abbott *et al.* (LIGO Scientific Collaboration), Setting upper limits on the strength of periodic gravitational waves from PSR J1939 + 213, Phys. Rev. D **69**, 082004 (2004).

[5] B. P. Abbott *et al.* (LIGO Scientific Collaboration), Limits on gravitational-wave emission from selected pulsars using LIGO data, Phys. Rev. Lett. **94**, 181103 (2005).

[6] B. P. Abbott *et al.* (LIGO Scientific Collaboration), Upper limits on gravitational wave emission from 78 radio pulsars, Phys. Rev. D **76**, 042001 (2007).

[7] B. P. Abbott *et al.* (LIGO Scientific Collaboration), Beating the spin-down limit on gravitational wave emission from the Crab pulsar, Astrophys. J. Lett. **683**, L45 (2008).

[8] B. P. Abbott *et al.* (LIGO Scientific and Virgo Collaborations), Searches for gravitational waves from known pulsars with S5 LIGO data, Astrophys. J. **713**, 671 (2010).

[9] S. J. Zhu *et al.*, Results of the deepest Einstein@Home search for continuous gravitational waves from CasA from the S6 LIGO Science Run, Phys. Rev. D **94**, 082008 (2016).

[10] J. Abadie *et al.* (LIGO Scientific Collaboration), First search for gravitational waves from the youngest known neutron star, Astrophys. J. **722**, 1504 (2010).

[11] J. Aasi *et al.* (LIGO Scientific and Virgo Collaborations), Searches for continuous gravitational waves from nine young supernova remnants, Astrophys. J. **813**, 39 (2015).

[12] B. P. Abbott *et al.* (LIGO Scientific and Virgo Collaborations), Search for continuous gravitational waves from neutron stars in globular cluster NGC 6544, arXiv:1607.02216.

[13] B. P. Abbott *et al.* (LIGO Scientific Collaboration), Searches for periodic gravitational waves from unknown isolated sources and Scorpius X-1: Results from the second LIGO science run, Phys. Rev. D **76**, 082001 (2007).

[14] B. P. Abbott *et al.* (LIGO Scientific Collaboration), First all-sky upper limits from LIGO on the strength of periodic gravitational waves using the Hough transform, Phys. Rev. D **72**, 102004 (2005).

[15] B. P. Abbott *et al.* (LIGO Scientific Collaboration), All-sky search for periodic gravitational waves in LIGO S4 data, Phys. Rev. D **77**, 022001 (2008).

[16] B. P. Abbott *et al.* (LIGO Scientific Collaboration), Einstein@Home search for periodic gravitational waves in LIGO S4 data, Phys. Rev. D **79**, 022001 (2009).

[17] B. P. Abbott *et al.* (LIGO Scientific Collaboration), All-sky LIGO Search for Periodic Gravitational Waves in the Early S5 Data, Phys. Rev. Lett. **102**, 111102 (2009).

[18] B. P. Abbott *et al.* (LIGO Scientific Collaboration), Einstein@Home search for periodic gravitational waves in early S5 LIGO data, Phys. Rev. D **80**, 042003 (2009).
[19] B. P. Abbott *et al.* (LIGO and Virgo Scientific Collaborations), All-sky search for periodic gravitational waves in the full S5 data, Phys. Rev. D **85**, 022001 (2012).
[20] B. P. Abbott *et al.* (LIGO Scientific Collaboration), Einstein@Home all-sky search for periodic gravitational waves in LIGO S5 data, Phys. Rev. D **87**, 042001 (2013).
[21] A. Singh, M. A. Papa, H.-B. Eggenstein, S. Zhu, H. Pletsch, B. Allen, O. Bock, B. Maschenchalk, R. Prix, and X. Siemens, Results of an all-sky high-frequency Einstein@ Home search for continuous gravitational waves in LIGO 5th Science Run, Phys. Rev. D **94**, 064061 (2016).
[22] J. Aasi *et al.* (LIGO Scientific and Virgo Collaborations), Comprehensive All-sky search for periodic gravitational waves in the Sixth Science Run LIGO data, Phys. Rev. D **94**, 042002 (2016).
[23] B. P. Abbott *et al.* (LIGO Scientific and Virgo Collaborations), Results of the deepest all-sky survey for continuous gravitational waves on LIGO S6 data running on the Einstein@Home volunteer distributed computing project, Phys. Rev. D **94**, 102002 (2016).
[24] J. Aasi *et al.* (LIGO Scientific and Virgo Collaborations), First low frequency all-sky search for continuous gravitational wave signals, Phys. Rev. D **93**, 042007 (2016).
[25] J. Aasi *et al.* (LIGO Scientific and Virgo Collaborations), A search of the Orion spur for continuous gravitational waves using a "loosely coherent" algorithm on data from LIGO interferometers, Phys. Rev. D **93**, 042006 (2016).
[26] J. Aasi *et al.* (LIGO Scientific and Virgo Collaborations), Application of a Hough search for continuous gravitational waves on data from the 5th LIGO science run, Classical Quantum Gravity **31**, 085014 (2014).
[27] J. Aasi *et al.* (LIGO Scientific and Virgo Collaborations), Implementation of an $\mathcal{F}$-statistic all-sky search for continuous gravitational waves in Virgo VSR1 data, Classical Quantum Gravity **31**, 165014 (2014).
[28] B. P. Abbott *et al.* (LIGO Scientific and Virgo Collaborations), First search for gravitational waves from known pulsars with Advanced LIGO, Astrophys. J. **839**, 12 (2017); Erratum, **851**, 71(E) (2017).
[29] B. P. Abbott *et al.* (LIGO Scientific and Virgo Collaborations), Directional Limits on Persistent Gravitational Waves from Advanced LIGOs First Observing Run, Phys. Rev. Lett. **118**, 121102 (2017).
[30] B. P. Abbott *et al.* (LIGO Scientific and Virgo Collaborations), First low-frequency Einstein@Home all-sky search for continuous gravitational waves in Advanced LIGO data, Phys. Rev. D **96**, 122004 (2017).
[31] B. P. Abbott *et al.* (LIGO Scientific and Virgo Collaborations), All-sky search for periodic gravitational waves in the O1 LIGO data, Phys. Rev. D **96**, 062002 (2017).
[32] M. A. Papa *et al.*, Hierarchical follow-up of subthreshold candidates of an all-sky Einstein@Home search for continuous gravitational waves on LIGO sixth science run data, Phys. Rev. D **94**, 122006 (2016).
[33] V. Dergachev, On blind searches for noise dominated signals: A loosely coherent approach, Classical Quantum Gravity **27**, 205017 (2010).
[34] V. Dergachev, A novel universal statistic for computing upper limits in ill-behaved background, Phys. Rev. D **87**, 062001 (2013).
[35] V. Dergachev, Error bounds for convolutional codes and an asymptotically optimum decoding algorithm, IEEE Trans. Inf. Theory **13**, 260 (1967).
[36] B. P. Abbott *et al.* (LIGO Scientific and Virgo Collaborations), Search for gravitational waves from Scorpius X-1 in the first Advanced LIGO observing run with a hidden Markov model, Phys. Rev. D **95**, 122003 (2017).
[37] S. Walsh *et al.*, A comparison of methods for the detection of gravitational waves from unknown neutron stars, Phys. Rev. D **94**, 124010 (2016).
[38] P. Jaranowski, A. Królak, and B. F. Schutz, Data analysis of gravitational-wave signals from spinning neutron stars. I. The signal and its detection, Phys. Rev. D **58**, 063001 (1998).
[39] See Supplemental Material at http://link.aps.org/supplemental/10.1103/PhysRevD.97.102003 for numerical values of upper limits.
[40] J. Aasi *et al.* (LIGO Scientific and Virgo Collaborations), Advanced LIGO, Classical Quantum Gravity **32**, 074001 (2015).
[41] B. P. Abbott *et al.* (LIGO Scientific and Virgo Collaborations), Maximum Elastic Deformations of Relativistic Stars, Phys. Rev. Lett. **116**, 131103 (2016).
[42] B. P. Abbott *et al.* (LIGO Scientific and Virgo Collaborations), Upper Limits on the Stochastic Gravitational-Wave Background from Advanced LIGO's First Observing Run, Phys. Rev. Lett. **118**, 121101 (2017).
[43] P. B. Covas *et al.*, https://dcc.ligo.org/LIGO-P1700440 (unpublished).
[44] V. Dergachev, LIGO Technical Document Report No. LIGO-T050186, 2005, https://dcc.ligo.org/.
[45] V. Dergachev, LIGO Technical Document Report No. LIGO-T1000272, 2010, https://dcc.ligo.org/.
[46] V. Dergachev and K. Riles, LIGO Technical Document Report No. LIGO-T050187, 2005, https://dcc.ligo.org/.
[47] V. Dergachev, Loosely coherent searches for sets of well-modeled signals, Phys. Rev. D **85**, 062003 (2012).
[48] B. P. Abbott *et al.* (LIGO Scientific and Virgo Collaborations), A Novel Universal Statistic for Computing Upper Limits in Ill-behaved Background, Phys. Rev. Lett. **120**, 031104 (2018).
[49] B. Krishnan, A. M. Sintes, M. A. Papa, B. F. Schutz, S. Frasca, and C. Palomba, The Hough transform search for continuous gravitational waves, Phys. Rev. D **70**, 082001 (2004).
[50] A. M. Sintes and B. Krishnan, Improved Hough search for gravitational wave pulsars, J. Phys. Conf. Ser. **32**, 20611 (2006).
[51] L Sancho de la Jordana and A. M. Sintes, A χ^2 veto for continuous gravitational wave searches, Classical Quantum Gravity **25**, 184014 (2008).
[52] B. Behnke, M. A. Papa, and R. Prix, A comparison of methods for the detection of gravitational waves from unknown neutron stars, Phys. Rev. D **91**, 064007 (2015).
[53] P. Astone, K. M. Borkowski, P. Jaranowski, M. Pietka, and A. Królak, Data analysis of gravitational-wave signals from

spinning neutron stars. V. A narrow-band all-sky search, Phys. Rev. D **82**, 022005 (2010).
[54] A. Pisarski and P. Jaranowski, Banks of templates for all-sky narrow-band searches of gravitational waves from spinning neutron stars, Classical Quantum Gravity **32**, 145014 (2015).
[55] C. J. Horowitz and K. Kadau, Breaking Strain of Neutron Star Crust and Gravitational Waves, Phys. Rev. Lett. **102**, 191102 (2009).
[56] N. K. Johnson-McDaniel and B. J. Owen, Maximum elastic deformations of relativistic stars, Phys. Rev. D **88**, 044004 (2013).

B. P. Abbott,[1] R. Abbott,[1] T. D. Abbott,[2] F. Acernese,[3,4] K. Ackley,[5,6] C. Adams,[7] T. Adams,[8] P. Addesso,[9] R. X. Adhikari,[1] V. B. Adya,[10] C. Affeldt,[10] M. Afrough,[11] B. Agarwal,[12] M. Agathos,[13] K. Agatsuma,[14] N. Aggarwal,[15] O. D. Aguiar,[16] L. Aiello,[17,18] A. Ain,[19] B. Allen,[10,20,21] G. Allen,[12] A. Allocca,[22,23] P. A. Altin,[24] A. Amato,[25] A. Ananyeva,[1] S. B. Anderson,[1] W. G. Anderson,[20] S. V. Angelova,[26] S. Antier,[27] S. Appert,[1] K. Arai,[1] M. C. Araya,[1] J. S. Areeda,[28] N. Arnaud,[27,29] S. Ascenzi,[30,31] G. Ashton,[10] M. Ast,[32] S. M. Aston,[7] P. Astone,[33] D. V. Atallah,[34] P. Aufmuth,[21] C. Aulbert,[10] K. AultONeal,[35] C. Austin,[2] A. Avila-Alvarez,[28] S. Babak,[36] P. Bacon,[37] M. K. M. Bader,[14] S. Bae,[38] P. T. Baker,[39] F. Baldaccini,[40,41] G. Ballardin,[29] S. W. Ballmer,[42] S. Banagiri,[43] J. C. Barayoga,[1] S. E. Barclay,[44] B. C. Barish,[1] D. Barker,[45] K. Barkett,[46] F. Barone,[3,4] B. Barr,[44] L. Barsotti,[15] M. Barsuglia,[37] D. Barta,[47] J. Bartlett,[45] I. Bartos,[48,5] R. Bassiri,[49] A. Basti,[22,23] J. C. Batch,[45] M. Bawaj,[50,41] J. C. Bayley,[44] M. Bazzan,[51,52] B. Bécsy,[53] C. Beer,[10] M. Bejger,[54] I. Belahcene,[27] A. S. Bell,[44] B. K. Berger,[1] G. Bergmann,[10] J. J. Bero,[55] C. P. L. Berry,[56] D. Bersanetti,[57] A. Bertolini,[14] J. Betzwieser,[7] S. Bhagwat,[42] R. Bhandare,[58] I. A. Bilenko,[59] G. Billingsley,[1] C. R. Billman,[5] J. Birch,[7] R. Birney,[60] O. Birnholtz,[10] S. Biscans,[1,15] S. Biscoveanu,[61,6] A. Bisht,[21] M. Bitossi,[29,23] C. Biwer,[42] M. A. Bizouard,[27] J. K. Blackburn,[1] J. Blackman,[46] C. D. Blair,[1,62] D. G. Blair,[62] R. M. Blair,[45] S. Bloemen,[63] O. Bock,[10] N. Bode,[10] M. Boer,[64] G. Bogaert,[64] A. Bohe,[36] F. Bondu,[65] E. Bonilla,[49] R. Bonnand,[8] B. A. Boom,[14] R. Bork,[1] V. Boschi,[29,23] S. Bose,[66,19] K. Bossie,[7] Y. Bouffanais,[37] A. Bozzi,[29] C. Bradaschia,[23] P. R. Brady,[20] M. Branchesi,[17,18] J. E. Brau,[67] T. Briant,[68] A. Brillet,[64] M. Brinkmann,[10] V. Brisson,[27] P. Brockill,[20] J. E. Broida,[69] A. F. Brooks,[1] D. A. Brown,[42] D. D. Brown,[70] S. Brunett,[1] C. C. Buchanan,[2] A. Buikema,[15] T. Bulik,[71] H. J. Bulten,[72,14] A. Buonanno,[36,73] D. Buskulic,[8] C. Buy,[37] R. L. Byer,[49] M. Cabero,[10] L. Cadonati,[74] G. Cagnoli,[25,75] C. Cahillane,[1] J. Calderón Bustillo,[74] T. A. Callister,[1] E. Calloni,[76,4] J. B. Camp,[77] M. Canepa,[78,57] P. Canizares,[63] K. C. Cannon,[79] H. Cao,[70] J. Cao,[80] C. D. Capano,[10] E. Capocasa,[37] F. Carbognani,[29] S. Caride,[81] M. F. Carney,[82] J. Casanueva Diaz,[27] C. Casentini,[30,31] S. Caudill,[20,14] M. Cavaglià,[11] F. Cavalier,[27] R. Cavalieri,[29] G. Cella,[23] C. B. Cepeda,[1] P. Cerdá-Durán,[83] G. Cerretani,[22,23] E. Cesarini,[84,31] S. J. Chamberlin,[61] M. Chan,[44] S. Chao,[85] P. Charlton,[86] E. Chase,[87] E. Chassande-Mottin,[37] D. Chatterjee,[20] B. D. Cheeseboro,[39] H. Y. Chen,[88] X. Chen,[62] Y. Chen,[46] H.-P. Cheng,[5] H. Y. Chia,[5] A. Chincarini,[57] A. Chiummo,[29] T. Chmiel,[82] H. S. Cho,[89] M. Cho,[73] J. H. Chow,[24] N. Christensen,[69,64] Q. Chu,[62] A. J. K. Chua,[13] S. Chua,[68] A. K. W. Chung,[90] S. Chung,[62] G. Ciani,[5,51,52] P. Ciecielag,[54] R. Ciolfi,[91,92] C. E. Cirelli,[49] A. Cirone,[78,57] F. Clara,[45] J. A. Clark,[74] P. Clearwater,[93] F. Cleva,[64] C. Cocchieri,[11] E. Coccia,[17,18] P.-F. Cohadon,[68] D. Cohen,[27] A. Colla,[94,33] C. G. Collette,[95] L. R. Cominsky,[96] M. Constancio Jr.,[16] L. Conti,[52] S. J. Cooper,[56] P. Corban,[7] T. R. Corbitt,[2] I. Cordero-Carrión,[97] K. R. Corley,[48] N. Cornish,[98] A. Corsi,[81] S. Cortese,[29] C. A. Costa,[16] E. T. Coughlin,[69] M. W. Coughlin,[69,1] S. B. Coughlin,[87] J.-P. Coulon,[64] S. T. Countryman,[48] P. Couvares,[1] P. B. Covas,[99] E. E. Cowan,[74] D. M. Coward,[62] M. J. Cowart,[7] D. C. Coyne,[1] R. Coyne,[81] J. D. E. Creighton,[20] T. D. Creighton,[100] J. Cripe,[2] S. G. Crowder,[101] T. J. Cullen,[28,2] A. Cumming,[44] L. Cunningham,[44] E. Cuoco,[29] T. Dal Canton,[77] G. Dálya,[53] S. L. Danilishin,[21,10] S. D'Antonio,[31] K. Danzmann,[21,10] A. Dasgupta,[102] C. F. Da Silva Costa,[5] V. Dattilo,[29] I. Dave,[58] M. Davier,[27] D. Davis,[42] E. J. Daw,[103] B. Day,[74] S. De,[42] D. DeBra,[49] J. Degallaix,[25] M. De Laurentis,[17,4] S. Deléglise,[68] W. Del Pozzo,[56,22,23] N. Demos,[15] T. Denker,[10] T. Dent,[10] R. De Pietri,[104,105] V. Dergachev,[36] R. De Rosa,[76,4] R. T. DeRosa,[7] C. De Rossi,[25,29] R. DeSalvo,[106] O. de Varona,[10] J. Devenson,[26] S. Dhurandhar,[19] M. C. Díaz,[100] L. Di Fiore,[4] M. Di Giovanni,[107,92] T. Di Girolamo,[48,76,4] A. Di Lieto,[22,23] S. Di Pace,[94,33] I. Di Palma,[94,33] F. Di Renzo,[22,23] Z. Doctor,[88] V. Dolique,[25] F. Donovan,[15] K. L. Dooley,[11] S. Doravari,[10] O. Dorosh,[108] I. Dorrington,[34] R. Douglas,[44] M. Dovale Álvarez,[56] T. P. Downes,[20] M. Drago,[10] C. Dreissigacker,[10] J. C. Driggers,[45] Z. Du,[80] M. Ducrot,[8] P. Dupej,[44] S. E. Dwyer,[45] T. B. Edo,[103] M. C. Edwards,[69] A. Effler,[7] H.-B. Eggenstein,[36,10] P. Ehrens,[1] J. Eichholz,[1] S. S. Eikenberry,[5]

R. A. Eisenstein,[15] R. C. Essick,[15] D. Estevez,[8] Z. B. Etienne,[39] T. Etzel,[1] M. Evans,[15] T. M. Evans,[7] M. Factourovich,[48] V. Fafone,[30,31,17] H. Fair,[42] S. Fairhurst,[34] X. Fan,[80] S. Farinon,[57] B. Farr,[88] W. M. Farr,[56] E. J. Fauchon-Jones,[34] M. Favata,[109] M. Fays,[34] C. Fee,[82] H. Fehrmann,[10] J. Feicht,[1] M. M. Fejer,[49] A. Fernandez-Galiana,[15] I. Ferrante,[22,23] E. C. Ferreira,[16] F. Ferrini,[29] F. Fidecaro,[22,23] D. Finstad,[42] I. Fiori,[29] D. Fiorucci,[37] M. Fishbach,[88] R. P. Fisher,[42] M. Fitz-Axen,[43] R. Flaminio,[25,110] M. Fletcher,[44] H. Fong,[111] J. A. Font,[83,112] P. W. F. Forsyth,[24] S. S. Forsyth,[74] J.-D. Fournier,[64] S. Frasca,[94,33] F. Frasconi,[23] Z. Frei,[53] A. Freise,[56] R. Frey,[67] V. Frey,[27] E. M. Fries,[1] P. Fritschel,[15] V. V. Frolov,[7] P. Fulda,[5] M. Fyffe,[7] H. Gabbard,[44] B. U. Gadre,[19] S. M. Gaebel,[56] J. R. Gair,[113] L. Gammaitoni,[40] M. R. Ganija,[70] S. G. Gaonkar,[19] C. Garcia-Quiros,[99] F. Garufi,[76,4] B. Gateley,[45] S. Gaudio,[35] G. Gaur,[114] V. Gayathri,[115] N. Gehrels,[77,†] G. Gemme,[57] E. Genin,[29] A. Gennai,[23] D. George,[12] J. George,[58] L. Gergely,[116] V. Germain,[8] S. Ghonge,[74] Abhirup Ghosh,[117] Archisman Ghosh,[117,14] S. Ghosh,[63,14,20] J. A. Giaime,[2,7] K. D. Giardina,[7] A. Giazotto,[23] K. Gill,[35] L. Glover,[106] E. Goetz,[118] R. Goetz,[5] S. Gomes,[34] B. Goncharov,[6] G. González,[2] J. M. Gonzalez Castro,[22,23] A. Gopakumar,[119] M. L. Gorodetsky,[59] S. E. Gossan,[1] M. Gosselin,[29] R. Gouaty,[8] A. Grado,[120,4] C. Graef,[44] M. Granata,[25] A. Grant,[44] S. Gras,[15] C. Gray,[45] G. Greco,[121,122] A. C. Green,[56] E. M. Gretarsson,[35] P. Groot,[63] H. Grote,[10] S. Grunewald,[36] P. Gruning,[27] G. M. Guidi,[121,122] X. Guo,[80] A. Gupta,[61] M. K. Gupta,[102] K. E. Gushwa,[1] E. K. Gustafson,[1] R. Gustafson,[118] O. Halim,[18,17] B. R. Hall,[66] E. D. Hall,[15] E. Z. Hamilton,[34] G. Hammond,[44] M. Haney,[123] M. M. Hanke,[10] J. Hanks,[45] C. Hanna,[61] M. D. Hannam,[34] O. A. Hannuksela,[90] J. Hanson,[7] T. Hardwick,[2] J. Harms,[17,18] G. M. Harry,[124] I. W. Harry,[36] M. J. Hart,[44] C.-J. Haster,[111] K. Haughian,[44] J. Healy,[55] A. Heidmann,[68] M. C. Heintze,[7] H. Heitmann,[64] P. Hello,[27] G. Hemming,[29] M. Hendry,[44] I. S. Heng,[44] J. Hennig,[44] A. W. Heptonstall,[1] M. Heurs,[10,21] S. Hild,[44] T. Hinderer,[63] D. Hoak,[29] D. Hofman,[25] K. Holt,[7] D. E. Holz,[88] P. Hopkins,[34] C. Horst,[20] J. Hough,[44] E. A. Houston,[44] E. J. Howell,[62] A. Hreibi,[64] Y. M. Hu,[10] E. A. Huerta,[12] D. Huet,[27] B. Hughey,[35] S. Husa,[99] S. H. Huttner,[44] T. Huynh-Dinh,[7] N. Indik,[10] R. Inta,[81] G. Intini,[94,33] H. N. Isa,[44] J.-M. Isac,[68] M. Isi,[1] B. R. Iyer,[117] K. Izumi,[45] T. Jacqmin,[68] K. Jani,[74] P. Jaranowski,[125] S. Jawahar,[60] F. Jiménez-Forteza,[99] W. W. Johnson,[2] D. I. Jones,[126] R. Jones,[44] R. J. G. Jonker,[14] L. Ju,[62] J. Junker,[10] C. V. Kalaghatgi,[34] V. Kalogera,[87] B. Kamai,[1] S. Kandhasamy,[7] G. Kang,[38] J. B. Kanner,[1] S. J. Kapadia,[20] S. Karki,[67] K. S. Karvinen,[10] M. Kasprzack,[2] M. Katolik,[12] E. Katsavounidis,[15] W. Katzman,[7] S. Kaufer,[21] K. Kawabe,[45] F. Kéfélian,[64] D. Keitel,[44] A. J. Kemball,[12] R. Kennedy,[103] C. Kent,[34] J. S. Key,[127] F. Y. Khalili,[59] I. Khan,[17,31] S. Khan,[10] Z. Khan,[102] E. A. Khazanov,[128] N. Kijbunchoo,[24] Chunglee Kim,[129] J. C. Kim,[130] K. Kim,[90] W. Kim,[70] W. S. Kim,[131] Y. -M. Kim,[89] S. J. Kimbrell,[74] E. J. King,[70] P. J. King,[45] M. Kinley-Hanlon,[124] R. Kirchhoff,[10] J. S. Kissel,[45] L. Kleybolte,[32] S. Klimenko,[5] T. D. Knowles,[39] P. Koch,[10] S. M. Koehlenbeck,[10] S. Koley,[14] V. Kondrashov,[1] A. Kontos,[15] M. Korobko,[32] W. Z. Korth,[1] I. Kowalska,[71] D. B. Kozak,[1] C. Krämer,[10] V. Kringel,[10] B. Krishnan,[10] A. Królak,[108,132] G. Kuehn,[10] P. Kumar,[111] R. Kumar,[102] S. Kumar,[117] L. Kuo,[85] A. Kutynia,[108] S. Kwang,[20] B. D. Lackey,[36] K. H. Lai,[90] M. Landry,[45] R. N. Lang,[133] J. Lange,[55] B. Lantz,[49] R. K. Lanza,[15] A. Lartaux-Vollard,[27] P. D. Lasky,[6] M. Laxen,[7] A. Lazzarini,[1] C. Lazzaro,[52] P. Leaci,[94,33] S. Leavey,[44] C. H. Lee,[89] H. K. Lee,[134] H. M. Lee,[135] H. W. Lee,[130] K. Lee,[44] J. Lehmann,[10] A. Lenon,[39] M. Leonardi,[107,92] N. Leroy,[27] N. Letendre,[8] Y. Levin,[6] T. G. F. Li,[90] S. D. Linker,[106] T. B. Littenberg,[136] J. Liu,[62] R. K. L. Lo,[90] N. A. Lockerbie,[60] L. T. London,[34] J. E. Lord,[42] M. Lorenzini,[17,18] V. Loriette,[137] M. Lormand,[7] G. Losurdo,[23] J. D. Lough,[10] G. Lovelace,[28] H. Lück,[21,10] D. Lumaca,[30,31] A. P. Lundgren,[10] R. Lynch,[15] Y. Ma,[46] R. Macas,[34] S. Macfoy,[26] B. Machenschalk,[10] M. MacInnis,[15] D. M. Macleod,[34] I. Magaña Hernandez,[20] F. Magaña-Sandoval,[42] L. Magaña Zertuche,[42] R. M. Magee,[61] E. Majorana,[33] I. Maksimovic,[137] N. Man,[64] V. Mandic,[43] V. Mangano,[44] G. L. Mansell,[24] M. Manske,[20,24] M. Mantovani,[29] F. Marchesoni,[50,41] F. Marion,[8] S. Márka,[48] Z. Márka,[48] C. Markakis,[12] A. S. Markosyan,[49] A. Markowitz,[1] E. Maros,[1] A. Marquina,[97] F. Martelli,[121,122] L. Martellini,[64] I. W. Martin,[44] R. M. Martin,[109] D. V. Martynov,[15] K. Mason,[15] E. Massera,[103] A. Masserot,[8] T. J. Massinger,[1] M. Masso-Reid,[44] S. Mastrogiovanni,[94,33] A. Matas,[43] F. Matichard,[1,15] L. Matone,[48] N. Mavalvala,[15] N. Mazumder,[66] R. McCarthy,[45] D. E. McClelland,[24] S. McCormick,[7] L. McCuller,[15] S. C. McGuire,[138] G. McIntyre,[1] J. McIver,[1] D. J. McManus,[24] L. McNeill,[6] T. McRae,[24] S. T. McWilliams,[39] D. Meacher,[61] G. D. Meadors,[36,10] M. Mehmet,[10] J. Meidam,[14] E. Mejuto-Villa,[9] A. Melatos,[93] G. Mendell,[45] R. A. Mercer,[20] E. L. Merilh,[45] M. Merzougui,[64] S. Meshkov,[1] C. Messenger,[44] C. Messick,[61] R. Metzdorff,[68] P. M. Meyers,[43] H. Miao,[56] C. Michel,[25] H. Middleton,[56] E. E. Mikhailov,[139] L. Milano,[76,4] A. L. Miller,[5,94,33] B. B. Miller,[87] J. Miller,[15] M. Millhouse,[98] M. C. Milovich-Goff,[106] O. Minazzoli,[64,140] Y. Minenkov,[31] J. Ming,[36] C. Mishra,[141] S. Mitra,[19] V. P. Mitrofanov,[59] G. Mitselmakher,[5] R. Mittleman,[15] D. Moffa,[82] A. Moggi,[23] K. Mogushi,[11] M. Mohan,[29] S. R. P. Mohapatra,[15] M. Montani,[121,122] C. J. Moore,[13] D. Moraru,[45] G. Moreno,[45]

S. R. Morriss,[100] B. Mours,[8] C. M. Mow-Lowry,[56] G. Mueller,[5] A. W. Muir,[34] Arunava Mukherjee,[10] D. Mukherjee,[20] S. Mukherjee,[100] N. Mukund,[19] A. Mullavey,[7] J. Munch,[70] E. A. Muñiz,[42] M. Muratore,[35] P. G. Murray,[44] K. Napier,[74] I. Nardecchia,[30,31] L. Naticchioni,[94,33] R. K. Nayak,[142] J. Neilson,[106] G. Nelemans,[63,14] T. J. N. Nelson,[7] M. Nery,[10] A. Neunzert,[118] L. Nevin,[1] J. M. Newport,[124] G. Newton,[44] K. Y. Ng,[90] T. T. Nguyen,[24] D. Nichols,[63] A. B. Nielsen,[10] S. Nissanke,[63,14] A. Nitz,[10] A. Noack,[10] F. Nocera,[29] D. Nolting,[7] C. North,[34] L. K. Nuttall,[34] J. Oberling,[45] G. D. O'Dea,[106] G. H. Ogin,[143] J. J. Oh,[131] S. H. Oh,[131] F. Ohme,[10] M. A. Okada,[16] M. Oliver,[99] P. Oppermann,[10] Richard J. Oram,[7] B. O'Reilly,[7] R. Ormiston,[43] L. F. Ortega,[5] R. O'Shaughnessy,[55] S. Ossokine,[36] D. J. Ottaway,[70] H. Overmier,[7] B. J. Owen,[81] A. E. Pace,[61] J. Page,[136] M. A. Page,[62] A. Pai,[115,144] S. A. Pai,[58] J. R. Palamos,[67] O. Palashov,[128] C. Palomba,[33] A. Pal-Singh,[32] Howard Pan,[85] Huang-Wei Pan,[85] B. Pang,[46] P. T. H. Pang,[90] C. Pankow,[87] F. Pannarale,[34] B. C. Pant,[58] F. Paoletti,[23] A. Paoli,[29] M. A. Papa,[36,20,10] A. Parida,[19] W. Parker,[7] D. Pascucci,[44] A. Pasqualetti,[29] R. Passaquieti,[22,23] D. Passuello,[23] M. Patil,[132] B. Patricelli,[145,23] B. L. Pearlstone,[44] M. Pedraza,[1] R. Pedurand,[25,146] L. Pekowsky,[42] A. Pele,[7] S. Penn,[147] C. J. Perez,[45] A. Perreca,[1,107,92] L. M. Perri,[87] H. P. Pfeiffer,[111,36] M. Phelps,[44] O. J. Piccinni,[94,33] M. Pichot,[64] F. Piergiovanni,[121,122] V. Pierro,[9] G. Pillant,[29] L. Pinard,[25] I. M. Pinto,[9] M. Pirello,[45] A. Pisarski,[125] M. Pitkin,[44] M. Poe,[20] R. Poggiani,[22,23] P. Popolizio,[29] E. K. Porter,[37] A. Post,[10] J. Powell,[148] J. Prasad,[19] J. W. W. Pratt,[35] G. Pratten,[99] V. Predoi,[34] T. Prestegard,[20] M. Prijatelj,[10] M. Principe,[9] S. Privitera,[36] G. A. Prodi,[107,92] L. G. Prokhorov,[59] O. Puncken,[10] M. Punturo,[41] P. Puppo,[33] M. Pürrer,[36] H. Qi,[20] V. Quetschke,[100] E. A. Quintero,[1] R. Quitzow-James,[67] F. J. Raab,[45] D. S. Rabeling,[24] H. Radkins,[45] P. Raffai,[53] S. Raja,[58] C. Rajan,[58] B. Rajbhandari,[81] M. Rakhmanov,[100] K. E. Ramirez,[100] A. Ramos-Buades,[99] P. Rapagnani,[94,33] V. Raymond,[36] M. Razzano,[22,23] J. Read,[28] T. Regimbau,[64] L. Rei,[57] S. Reid,[60] D. H. Reitze,[1,5] W. Ren,[12] S. D. Reyes,[42] F. Ricci,[94,33] P. M. Ricker,[12] S. Rieger,[10] K. Riles,[118] M. Rizzo,[55] N. A. Robertson,[1,44] R. Robie,[44] F. Robinet,[27] A. Rocchi,[31] L. Rolland,[8] J. G. Rollins,[1] V. J. Roma,[67] R. Romano,[3,4] C. L. Romel,[45] J. H. Romie,[7] D. Rosińska,[149,54] M. P. Ross,[150] S. Rowan,[44] A. Rüdiger,[10] P. Ruggi,[29] G. Rutins,[26] K. Ryan,[45] S. Sachdev,[1] T. Sadecki,[45] L. Sadeghian,[20] M. Sakellariadou,[151] L. Salconi,[29] M. Saleem,[115] F. Salemi,[10] A. Samajdar,[142] L. Sammut,[6] L. M. Sampson,[87] E. J. Sanchez,[1] L. E. Sanchez,[1] N. Sanchis-Gual,[83] V. Sandberg,[45] J. R. Sanders,[42] B. Sassolas,[25] P. R. Saulson,[42] O. Sauter,[118] R. L. Savage,[45] A. Sawadsky,[32] P. Schale,[67] M. Scheel,[46] J. Scheuer,[87] J. Schmidt,[10] P. Schmidt,[1,63] R. Schnabel,[32] R. M. S. Schofield,[67] A. Schönbeck,[32] E. Schreiber,[10] D. Schuette,[10,21] B. W. Schulte,[10] B. F. Schutz,[34,10] S. G. Schwalbe,[35] J. Scott,[44] S. M. Scott,[24] E. Seidel,[12] D. Sellers,[7] A. S. Sengupta,[152] D. Sentenac,[29] V. Sequino,[30,31,17] A. Sergeev,[128] D. A. Shaddock,[24] T. J. Shaffer,[45] A. A. Shah,[136] M. S. Shahriar,[87] M. B. Shaner,[106] L. Shao,[36] B. Shapiro,[49] P. Shawhan,[73] A. Sheperd,[20] D. H. Shoemaker,[15] D. M. Shoemaker,[74] K. Siellez,[74] X. Siemens,[20] M. Sieniawska,[54] D. Sigg,[45] A. D. Silva,[16] L. P. Singer,[77] A. Singh,[36,10,21] A. Singhal,[17,33] A. M. Sintes,[99] B. J. J. Slagmolen,[24] B. Smith,[7] J. R. Smith,[28] R. J. E. Smith,[1,6] S. Somala,[153] E. J. Son,[131] J. A. Sonnenberg,[20] B. Sorazu,[44] F. Sorrentino,[57] T. Souradeep,[19] A. P. Spencer,[44] A. K. Srivastava,[102] K. Staats,[35] A. Staley,[48] M. Steinke,[10] J. Steinlechner,[32,44] S. Steinlechner,[32] D. Steinmeyer,[10] S. P. Stevenson,[56,148] R. Stone,[100] D. J. Stops,[56] K. A. Strain,[44] G. Stratta,[121,122] S. E. Strigin,[59] A. Strunk,[45] R. Sturani,[154] A. L. Stuver,[7] T. Z. Summerscales,[155] L. Sun,[93] S. Sunil,[102] J. Suresh,[19] P. J. Sutton,[34] B. L. Swinkels,[29] M. J. Szczepańczyk,[35] M. Tacca,[14] S. C. Tait,[44] C. Talbot,[6] D. Talukder,[67] D. B. Tanner,[5] D. Tao,[69] M. Tápai,[116] A. Taracchini,[36] J. D. Tasson,[69] J. A. Taylor,[136] R. Taylor,[1] S. V. Tewari,[147] T. Theeg,[10] F. Thies,[10] E. G. Thomas,[56] M. Thomas,[7] P. Thomas,[45] K. A. Thorne,[7] E. Thrane,[6] S. Tiwari,[17,92] V. Tiwari,[34] K. V. Tokmakov,[60] K. Toland,[44] M. Tonelli,[22,23] Z. Tornasi,[44] A. Torres-Forné,[83] C. I. Torrie,[1] D. Töyrä,[56] F. Travasso,[29,41] G. Traylor,[7] J. Trinastic,[5] M. C. Tringali,[107,92] L. Trozzo,[156,23] K. W. Tsang,[14] M. Tse,[15] R. Tso,[1] L. Tsukada,[79] D. Tsuna,[79] D. Tuyenbayev,[100] K. Ueno,[20] D. Ugolini,[157] C. S. Unnikrishnan,[119] A. L. Urban,[1] S. A. Usman,[34] H. Vahlbruch,[21] G. Vajente,[1] G. Valdes,[2] N. van Bakel,[14] M. van Beuzekom,[14] J. F. J. van den Brand,[72,14] C. Van Den Broeck,[14,158] D. C. Vander-Hyde,[42] L. van der Schaaf,[14] J. V. van Heijningen,[14] A. A. van Veggel,[44] M. Vardaro,[51,52] V. Varma,[46] S. Vass,[1] M. Vasúth,[47] A. Vecchio,[56] G. Vedovato,[52] J. Veitch,[44] P. J. Veitch,[70] K. Venkateswara,[150] G. Venugopalan,[1] D. Verkindt,[8] F. Vetrano,[121,122] A. Viceré,[121,122] A. D. Viets,[20] S. Vinciguerra,[56] D. J. Vine,[26] J.-Y. Vinet,[64] S. Vitale,[15] T. Vo,[42] H. Vocca,[40,41] C. Vorvick,[45] S. P. Vyatchanin,[59] A. R. Wade,[1] L. E. Wade,[82] M. Wade,[82] R. Walet,[14] M. Walker,[28] L. Wallace,[1] S. Walsh,[36,10,20] G. Wang,[17,122] H. Wang,[56] J. Z. Wang,[61] W. H. Wang,[100] Y. F. Wang,[90] R. L. Ward,[24] J. Warner,[45] M. Was,[8] J. Watchi,[95] B. Weaver,[45] L.-W. Wei,[10,21] M. Weinert,[10] A. J. Weinstein,[1] R. Weiss,[15] L. Wen,[62] E. K. Wessel,[12] P. Weßels,[10] J. Westerweck,[10] T. Westphal,[10] K. Wette,[24] J. T. Whelan,[55] B. F. Whiting,[5] C. Whittle,[6] D. Wilken,[10] D. Williams,[44] R. D. Williams,[1] A. R. Williamson,[63] J. L. Willis,[1,159] B. Willke,[21,10] M. H. Wimmer,[10]

W. Winkler,[10] C. C. Wipf,[1] H. Wittel,[10,21] G. Woan,[44] J. Woehler,[10] J. Wofford,[55] W. K. Wong,[90] J. Worden,[45] J. L. Wright,[44] D. S. Wu,[10] D. M. Wysocki,[55] S. Xiao,[1] H. Yamamoto,[1] C. C. Yancey,[73] L. Yang,[160] M. J. Yap,[24] M. Yazback,[5] Hang Yu,[15] Haocun Yu,[15] M. Yvert,[8] A. Zadrożny,[108] M. Zanolin,[35] T. Zelenova,[29] J.-P. Zendri,[52] M. Zevin,[87] L. Zhang,[1] M. Zhang,[139] T. Zhang,[44] Y.-H. Zhang,[55] C. Zhao,[62] M. Zhou,[87] Z. Zhou,[87] S. J. Zhu,[36,10] X. J. Zhu,[6] M. E. Zucker,[1,15] and J. Zweizig[1]

(LIGO Scientific Collaboration and Virgo Collaboration)

[1]*LIGO, California Institute of Technology, Pasadena, California 91125, USA*
[2]*Louisiana State University, Baton Rouge, Louisiana 70803, USA*
[3]*Università di Salerno, Fisciano, I-84084 Salerno, Italy*
[4]*INFN, Sezione di Napoli, Complesso Universitario di Monte S.Angelo, I-80126 Napoli, Italy*
[5]*University of Florida, Gainesville, Florida 32611, USA*
[6]*OzGrav, School of Physics and Astronomy, Monash University, Clayton 3800, Victoria, Australia*
[7]*LIGO Livingston Observatory, Livingston, Louisiana 70754, USA*
[8]*Laboratoire d'Annecy-le-Vieux de Physique des Particules (LAPP), Université Savoie Mont Blanc, CNRS/IN2P3, F-74941 Annecy, France*
[9]*University of Sannio at Benevento, I-82100 Benevento, Italy and INFN, Sezione di Napoli, I-80100 Napoli, Italy*
[10]*Max Planck Institute for Gravitational Physics (Albert Einstein Institute), D-30167 Hannover, Germany*
[11]*The University of Mississippi, University, Mississippi 38677, USA*
[12]*NCSA, University of Illinois at Urbana-Champaign, Urbana, Illinois 61801, USA*
[13]*University of Cambridge, Cambridge CB2 1TN, United Kingdom*
[14]*Nikhef, Science Park, 1098 XG Amsterdam, Netherlands*
[15]*LIGO, Massachusetts Institute of Technology, Cambridge, Massachusetts 02139, USA*
[16]*Instituto Nacional de Pesquisas Espaciais, 12227-010 São José dos Campos, São Paulo, Brazil*
[17]*Gran Sasso Science Institute (GSSI), I-67100 L'Aquila, Italy*
[18]*INFN, Laboratori Nazionali del Gran Sasso, I-67100 Assergi, Italy*
[19]*Inter-University Centre for Astronomy and Astrophysics, Pune 411007, India*
[20]*University of Wisconsin-Milwaukee, Milwaukee, Wisconsin 53201, USA*
[21]*Leibniz Universität Hannover, D-30167 Hannover, Germany*
[22]*Università di Pisa, I-56127 Pisa, Italy*
[23]*INFN, Sezione di Pisa, I-56127 Pisa, Italy*
[24]*OzGrav, Australian National University, Canberra, Australian Capital Territory 0200, Australia*
[25]*Laboratoire des Matériaux Avancés (LMA), CNRS/IN2P3, F-69622 Villeurbanne, France*
[26]*SUPA, University of the West of Scotland, Paisley PA1 2BE, United Kingdom*
[27]*LAL, Univ. Paris-Sud, CNRS/IN2P3, Université Paris-Saclay, F-91898 Orsay, France*
[28]*California State University Fullerton, Fullerton, California 92831, USA*
[29]*European Gravitational Observatory (EGO), I-56021 Cascina, Pisa, Italy*
[30]*Università di Roma Tor Vergata, I-00133 Roma, Italy*
[31]*INFN, Sezione di Roma Tor Vergata, I-00133 Roma, Italy*
[32]*Universität Hamburg, D-22761 Hamburg, Germany*
[33]*INFN, Sezione di Roma, I-00185 Roma, Italy*
[34]*Cardiff University, Cardiff CF24 3AA, United Kingdom*
[35]*Embry-Riddle Aeronautical University, Prescott, Arizona 86301, USA*
[36]*Max Planck Institute for Gravitational Physics (Albert Einstein Institute), D-14476 Potsdam-Golm, Germany*
[37]*APC, AstroParticule et Cosmologie, Université Paris Diderot, CNRS/IN2P3, CEA/Irfu, Observatoire de Paris, Sorbonne Paris Cité, F-75205 Paris Cedex 13, France*
[38]*Korea Institute of Science and Technology Information, Daejeon 34141, Korea*
[39]*West Virginia University, Morgantown, West Virginia 26506, USA*
[40]*Università di Perugia, I-06123 Perugia, Italy*
[41]*INFN, Sezione di Perugia, I-06123 Perugia, Italy*
[42]*Syracuse University, Syracuse, New York 13244, USA*
[43]*University of Minnesota, Minneapolis, Minnesota 55455, USA*
[44]*SUPA, University of Glasgow, Glasgow G12 8QQ, United Kingdom*
[45]*LIGO Hanford Observatory, Richland, Washington 99352, USA*
[46]*Caltech CaRT, Pasadena, California 91125, USA*
[47]*Wigner RCP, RMKI, H-1121 Budapest, Konkoly Thege Miklós út 29-33, Hungary*
[48]*Columbia University, New York, New York 10027, USA*

[49]Stanford University, Stanford, California 94305, USA
[50]Università di Camerino, Dipartimento di Fisica, I-62032 Camerino, Italy
[51]Università di Padova, Dipartimento di Fisica e Astronomia, I-35131 Padova, Italy
[52]INFN, Sezione di Padova, I-35131 Padova, Italy
[53]Institute of Physics, Eötvös University, Pázmány P. s. 1/A, Budapest 1117, Hungary
[54]Nicolaus Copernicus Astronomical Center, Polish Academy of Sciences, 00-716 Warsaw, Poland
[55]Rochester Institute of Technology, Rochester, New York 14623, USA
[56]University of Birmingham, Birmingham B15 2TT, United Kingdom
[57]INFN, Sezione di Genova, I-16146 Genova, Italy
[58]RRCAT, Indore MP 452013, India
[59]Faculty of Physics, Lomonosov Moscow State University, Moscow 119991, Russia
[60]SUPA, University of Strathclyde, Glasgow G1 1XQ, United Kingdom
[61]The Pennsylvania State University, University Park, Pennsylvania 16802, USA
[62]OzGrav, University of Western Australia, Crawley, Western Australia 6009, Australia
[63]Department of Astrophysics/IMAPP, Radboud University Nijmegen, P.O. Box 9010, 6500 GL Nijmegen, Netherlands
[64]Artemis, Université Côte d'Azur, Observatoire Côte d'Azur, CNRS, CS 34229, F-06304 Nice Cedex 4, France
[65]Institut FOTON, CNRS, Université de Rennes 1, F-35042 Rennes, France
[66]Washington State University, Pullman, Washington 99164, USA
[67]University of Oregon, Eugene, Oregon 97403, USA
[68]Laboratoire Kastler Brossel, UPMC-Sorbonne Universités, CNRS, ENS-PSL Research University, Collège de France, F-75005 Paris, France
[69]Carleton College, Northfield, Minnesota 55057, USA
[70]OzGrav, University of Adelaide, Adelaide, South Australia 5005, Australia
[71]Astronomical Observatory Warsaw University, 00-478 Warsaw, Poland
[72]VU University Amsterdam, 1081 HV Amsterdam, Netherlands
[73]University of Maryland, College Park, Maryland 20742, USA
[74]School of Physics, Georgia Institute of Technology, Atlanta, Georgia 30332, USA
[75]Université Claude Bernard Lyon 1, F-69622 Villeurbanne, France
[76]Università di Napoli 'Federico II,' Complesso Universitario di Monte S.Angelo, I-80126 Napoli, Italy
[77]NASA Goddard Space Flight Center, Greenbelt, Maryland 20771, USA
[78]Dipartimento di Fisica, Università degli Studi di Genova, I-16146 Genova, Italy
[79]RESCEU, University of Tokyo, Tokyo 113-0033, Japan
[80]Tsinghua University, Beijing 100084, China
[81]Texas Tech University, Lubbock, Texas 79409, USA
[82]Kenyon College, Gambier, Ohio 43022, USA
[83]Departamento de Astronomía y Astrofísica, Universitat de València, E-46100 Burjassot, València, Spain
[84]Museo Storico della Fisica e Centro Studi e Ricerche Enrico Fermi, I-00184 Roma, Italy
[85]National Tsing Hua University, Hsinchu City, 30013 Taiwan, Republic of China
[86]Charles Sturt University, Wagga Wagga, New South Wales 2678, Australia
[87]Center for Interdisciplinary Exploration and Research in Astrophysics (CIERA), Northwestern University, Evanston, Illinois 60208, USA
[88]University of Chicago, Chicago, Illinois 60637, USA
[89]Pusan National University, Busan 46241, Korea
[90]The Chinese University of Hong Kong, Shatin, NT, Hong Kong
[91]INAF, Osservatorio Astronomico di Padova, I-35122 Padova, Italy
[92]INFN, Trento Institute for Fundamental Physics and Applications, I-38123 Povo, Trento, Italy
[93]OzGrav, University of Melbourne, Parkville, Victoria 3010, Australia
[94]Università di Roma 'La Sapienza,' I-00185 Roma, Italy
[95]Université Libre de Bruxelles, Brussels 1050, Belgium
[96]Sonoma State University, Rohnert Park, California 94928, USA
[97]Departamento de Matemáticas, Universitat de València, E-46100 Burjassot, València, Spain
[98]Montana State University, Bozeman, Montana 59717, USA
[99]Universitat de les Illes Balears, IAC3—IEEC, E-07122 Palma de Mallorca, Spain
[100]The University of Texas Rio Grande Valley, Brownsville, Texas 78520, USA
[101]Bellevue College, Bellevue, Washington 98007, USA
[102]Institute for Plasma Research, Bhat, Gandhinagar 382428, India
[103]The University of Sheffield, Sheffield S10 2TN, United Kingdom

[104]*Dipartimento di Scienze Matematiche, Fisiche e Informatiche, Università di Parma, I-43124 Parma, Italy*
[105]*INFN, Sezione di Milano Bicocca, Gruppo Collegato di Parma, I-43124 Parma, Italy*
[106]*California State University, Los Angeles, 5151 State University Dr, Los Angeles, California 90032, USA*
[107]*Università di Trento, Dipartimento di Fisica, I-38123 Povo, Trento, Italy*
[108]*NCBJ, 05-400 Świerk-Otwock, Poland*
[109]*Montclair State University, Montclair, New Jersey 07043, USA*
[110]*National Astronomical Observatory of Japan, 2-21-1 Osawa, Mitaka, Tokyo 181-8588, Japan*
[111]*Canadian Institute for Theoretical Astrophysics, University of Toronto, Toronto, Ontario M5S 3H8, Canada*
[112]*Observatori Astronòmic, Universitat de València, E-46980 Paterna, València, Spain*
[113]*School of Mathematics, University of Edinburgh, Edinburgh EH9 3FD, United Kingdom*
[114]*University and Institute of Advanced Research, Koba Institutional Area, Gandhinagar Gujarat 382007, India*
[115]*IISER-TVM, CET Campus, Trivandrum Kerala 695016, India*
[116]*University of Szeged, Dóm tér 9, Szeged 6720, Hungary*
[117]*International Centre for Theoretical Sciences, Tata Institute of Fundamental Research, Bengaluru 560089, India*
[118]*University of Michigan, Ann Arbor, Michigan 48109, USA*
[119]*Tata Institute of Fundamental Research, Mumbai 400005, India*
[120]*INAF, Osservatorio Astronomico di Capodimonte, I-80131 Napoli, Italy*
[121]*Università degli Studi di Urbino 'Carlo Bo,' I-61029 Urbino, Italy*
[122]*INFN, Sezione di Firenze, I-50019 Sesto Fiorentino, Firenze, Italy*
[123]*Physik-Institut, University of Zurich, Winterthurerstrasse 190, 8057 Zurich, Switzerland*
[124]*American University, Washington, D.C. 20016, USA*
[125]*University of Białystok, 15-424 Białystok, Poland*
[126]*University of Southampton, Southampton SO17 1BJ, United Kingdom*
[127]*University of Washington Bothell, 18115 Campus Way NE, Bothell, Washington 98011, USA*
[128]*Institute of Applied Physics, Nizhny Novgorod 603950, Russia*
[129]*Korea Astronomy and Space Science Institute, Daejeon 34055, Korea*
[130]*Inje University Gimhae, South Gyeongsang 50834, Korea*
[131]*National Institute for Mathematical Sciences, Daejeon 34047, Korea*
[132]*Institute of Mathematics, Polish Academy of Sciences, 00656 Warsaw, Poland*
[133]*Hillsdale College, Hillsdale, Michigan 49242, USA*
[134]*Hanyang University, Seoul 04763, Korea*
[135]*Seoul National University, Seoul 08826, Korea*
[136]*NASA Marshall Space Flight Center, Huntsville, Alabama 35811, USA*
[137]*ESPCI, CNRS, F-75005 Paris, France*
[138]*Southern University and A&M College, Baton Rouge, Louisiana 70813, USA*
[139]*College of William and Mary, Williamsburg, Virginia 23187, USA*
[140]*Centre Scientifique de Monaco, 8 quai Antoine Ier, MC-98000, Monaco*
[141]*Indian Institute of Technology Madras, Chennai 600036, India*
[142]*IISER-Kolkata, Mohanpur, West Bengal 741252, India*
[143]*Whitman College, 345 Boyer Avenue, Walla Walla, Washington 99362 USA*
[144]*Indian Institute of Technology Bombay, Powai, Mumbai, Maharashtra 400076, India*
[145]*Scuola Normale Superiore, Piazza dei Cavalieri 7, I-56126 Pisa, Italy*
[146]*Université de Lyon, F-69361 Lyon, France*
[147]*Hobart and William Smith Colleges, Geneva, New York 14456, USA*
[148]*OzGrav, Swinburne University of Technology, Hawthorn VIC 3122, Australia*
[149]*Janusz Gil Institute of Astronomy, University of Zielona Góra, 65-265 Zielona Góra, Poland*
[150]*University of Washington, Seattle, Washington 98195, USA*
[151]*King's College London, University of London, London WC2R 2LS, United Kingdom*
[152]*Indian Institute of Technology, Gandhinagar Ahmedabad Gujarat 382424, India*
[153]*Indian Institute of Technology Hyderabad, Sangareddy, Khandi, Telangana 502285, India*
[154]*International Institute of Physics, Universidade Federal do Rio Grande do Norte, Natal RN 59078-970, Brazil*
[155]*Andrews University, Berrien Springs, Michigan 49104, USA*
[156]*Università di Siena, I-53100 Siena, Italy*
[157]*Trinity University, San Antonio, Texas 78212, USA*

[158]*Van Swinderen Institute for Particle Physics and Gravity, University of Groningen, Nijenborgh 4, 9747 AG Groningen, Netherlands*
[159]*Abilene Christian University, Abilene, Texas 79699, USA*
[160]*Colorado State University, Fort Collins, Colorado 80523, USA*

[†]Deceased.